UNIVERSITY OF OKLAHOMA

GRADUATE COLLEGE

EFFECTS OF HEIGHT ABOVE BURNER AND OXYGEN CONTENT ON SOOT FORMATION AND NANOSTRUCTURE IN A CO-FLOW LAMINAR DIFFUSION FLAME FUELED WITH METHANE

A THESIS

SUBMITTED TO THE GRADUATE FACULTY

in partial fulfillment of the requirements for the

Degree of

MASTER OF SCIENCE

By

JACOB A. GEELS

Norman, Oklahoma

2025

EFFECTS OF HEIGHT ABOVE BURNER AND OXYGEN CONTENT ON SOOT FORMATION AND NANOSTRUCTURE IN A CO-FLOW LAMINAR DIFFUSION FLAME FUELED WITH METHANE

A THESIS APPROVED FOR THE

SCHOOL OF AEROSPACE AND MECHANICAL ENGINEERING

BY THE COMMITTEE CONSISTING OF

Dr. Wilson Merchan-Merchan, Chair

Dr. Ramkumar Parthasarathy

Dr. Jivtesh Garg

Dedication

To Debra Geels: my mother, my biggest fan, who always told me I was only limited by how big I could dream

Acknowledgments

I want to start by extending my gratitude to my advisor, Dr. Merchan-Merchan. He allowed me to join his research group and greatly facilitated my training. Thank you, sir, for your guidance and patience. Without your invaluable insight into the world of combustion, this thesis and the associated research would not have been possible. I would also like to thank Dr. Parthasarathy for his aid. He greatly assisted with my navigation of the curriculum and research during my tenure at OU. He also allowed me to be a teaching assistant for the AME department to support myself throughout my research. For this, I am forever grateful.

I would also like to thank my friends and family for all their support. Adam, Kyle, and John Thomas, I am indebted to you for the help with conceptualization and proofreading. Thank you for always being willing to be an ear to listen and a wall I can bounce ideas off. To my family, my father Patrick, sister Emily, brother Daniel, and mother Debra, who unfortunately passed during the writing of this thesis, thank you for always being my biggest fans and shaping me into the person I am. Lastly, I would like to give special thanks to my girlfriend for being at my side during this work. Faith, thank you for being patient with me during the long nights of writing and offering help interpreting statistics. I love you!

List of Figures

List of Tables

Table of Contents

Abstract

Soot is particulate matter that comes from the incomplete combustion of hydrocarbon fuels. It is a well-known respiratory irritant and can cause build-up in combustion equipment. For both reasons, soot mitigation strategies have become a topic of much research. One such method is known as oxygen-enhanced combustion, which is the practice of enriching the oxidizer stream in a combustion system to higher-than-air oxygen percentages. This has the benefit of reducing soot formation, leading to fewer emissions. This work aims to qualify and quantify the effect of a 100% oxygen oxidizer stream on the soot. This effect is being quantified by measurement of soot primary particle diameter, flame temperature, and soot nanostructure metrics such as fringe length, fringe tortuosity, and fringe lattice spacing gleaned from high-resolution TEM images. It is qualified by observation of soot particle population density and degree of agglomeration of aggregates from low and median resolution TEM images. It was found that methane/100% oxygen flames share similar trends to methane/air flames based on soot evolution, particle population density, degree of agglomeration, and primary particle density, but the values for these metrics are lower for the oxygen flame, suggesting increased oxidation and therefore less soot formation/growth. Soot nanostructure metrics for both flames showed little change with HAB, reinforcing the assertion that methane is a non-graphitizing fuel. It was also found that the only metric that changed with increased oxygen concentration was fringe length, suggesting that the apparent increase in structural order in soot produced by methane/100% oxygen flames is only due to an increase in graphitic plane length.

Chapter 1: Introduction

1.1 Background on Oxy Combustion

Combustion is vastly important in almost every aspect of life. Whether it be for power production, heating, or public/personal transportation, almost no one is completely isolated from combustion today. As of 2019, 81% of global power production was produced by the combustion of some hydrocarbons: coal, oil, and natural gas
[1]. Hydrocarbons are so popular due to their energy density and the relative ease of harvesting this energy. These chemicals can be ignited in the presence of oxygen or heated in the absence of oxygen, breaking them down into their constituents, releasing energy from the chemical bonds. Practical combustion systems use the former method, so that is what will primarily be discussed. When hydrocarbons are ignited, they require a certain amount of oxygen to be burned perfectly. This is known as the stoichiometric condition. In most practical combustion systems, air is used as an oxidizer. Due to this, there is often either not enough oxygen to fully oxidize the fuel, or due to the high volume of nitrogen in air (79%), the fuel particles do not have enough residence time in the flame to be exposed to enough oxygen to fully oxidize. This leads to incomplete combustion and the production of unwanted by-products. Soot is one such by-product, which is carbonaceous particles. These particles are known as respiratory irritants and play a large role in the radiant heat transfer of flames. [2]. Soot can also be considered a nuisance and can cause buildup in combustors and downstream components. An example of soot buildup can be seen in Figure 1.

Figure 1: Soot Build-Up in the Exhaust Manifold of a Diesel Engine [3]

Another unwanted consequence of combustion with air is the production of nitrogen oxides (NOx). While these chemicals are not directly produced by incomplete combustion, as with soot, incomplete combustion conditions increase their formation in processes that will be discussed in more detail later [2]. NOx is primarily formed in combustion with air due to high temperatures. The triple bond between the two nitrogen atoms in the diatomic molecule dissolves at high temperatures. This also happens with diatomic oxygen molecules and is known as dissociation. This allows the nitrogen, which is usually inert, to react with the oxygen from the air to produce NOx. NOx is known to be a contributor to acid rain and surface-level ozone, a main component of smog [4]. Because of the negative effects of these pollutants, much research has gone towards developing soot and NOx suppression techniques.

1.1.1 Advantages and Disadvantages of Oxy Combustion

As previously mentioned, most combustion systems use air as an oxidizer. This includes everything from a wood-burning stove to a turbojet engine on a passenger airliner, and everything in between. Air is often used due to convenience and cost. The air around us contains

around 78% nitrogen, 21% oxygen, and around 1% trace elements/compounds such as argon and carbon dioxide [5]. This 21% oxygen is readily available to react, removing the need for any kind of potentially expensive pre-processing, and is abundant, making it cost virtually nothing to utilize. These reasons make air a popular choice as an oxidizer, though it is not without its drawbacks. Due to the large percentage of nitrogen in the air, very high air-to-fuel ratios are required to have enough oxygen present to achieve complete combustion. For example, in the stoichiometric burning of 1 kilogram of methane, approximately 17.19 kilograms of air are required. This can require larger pumps and compressors to handle the larger mass flow rates, leading to higher costs. The presence of nitrogen can also lead to the formation of unwanted byproducts of combustion. Due to high combustion temperatures, nitrogen, a gas that is typically considered inert, dissociates from its naturally occurring diatomic state into two free nitrogen atoms. They can then react with the available oxygen molecules to form nitrogen oxides. These nitrogen oxides are known to have adverse health effects. The potential of incomplete combustion also has the downside of producing soot. Soot is also known to have adverse health effects.

Because of the potential adverse health effects of using air as an oxidizer, as well as the fact that less oxygen present leads to lower combustion temperatures and lower combustor efficiencies, researchers and engineers have tried a variety of methods to alleviate these issues. One example of this is the use of fuel additives to reduce the formation of unwanted by-products such as soot by promoting the oxidation of these particles before they are released. Another way is to utilize alternative fuels. Fuels chosen for this purpose typically are either simpler hydrocarbons, meaning they more readily oxidize, therefore leaving less chance to become soot precursors, or are biofuels that are chosen because they contain oxygen, which helps to reduce the chances of incomplete combustion [6]. Following the same reasoning for the selection of biofuels (more oxygen present reduces the chances of incomplete combustion), researchers have been investigating what is known as oxy combustion. This is a type of combustion where, instead of using ambient air as an oxidizer, the air is either supplemented with oxygen or pure oxygen is used. Numerous benefits come from such a technique. In either case, more oxygen is being provided to the reaction, meaning higher oxidation rates and more complete oxidation of hydrocarbon fuels. This leads to fewer precursors forming and therefore less soot. Another

benefit is that due to oxygen being added or being the sole oxidizer, nitrogen in the oxidizer stream is either reduced in percentage or eliminated, meaning that less is present to dissociate and react to become NOx. This can be seen in Equations 1 and 2.

$$CH_4 + 2(O_2 + 3.76\,N_2) \rightarrow CO_2 + 2H_2O + 7.52N_2 \quad (1)$$

$$CH_4 + 2(O_2\,) \rightarrow CO_2 + 2H_2O \quad (2)$$

Equation 1 represents the perfect combustion of one mole of methane with atmospheric air. As can be seen, on the right-hand side of this equation, there is residual nitrogen left over because of this reaction. In Equation 2, methane is still being burned, but pure oxygen is used instead of air. Because of this, no nitrogen is present in the reaction and therefore cannot later dissociate and form nitrogen oxides. Some other benefits to this method include its ability to be added to current combustor systems with little retrofitting of the primary system, no need for fuel reformulation, and increased thermal efficiency [7].

Although oxy combustion presents a variety of benefits and the ability to reduce soot and NOx, it is not without its drawbacks. For starters, even though NOx production is technically reduced by the increase in oxygen content displacing the nitrogen content in the oxidizer stream, due to the higher combustion temperatures that result from more complete combustion, dissociation of the nitrogen molecules that are present becomes increasingly likely [7]. This can result in a higher NOx output and can require additional NOx mitigation strategies that can be expensive to implement. There are also issues with the infrastructure involved. While many combustion systems can begin to utilize oxy combustion without many modifications, there is still a need for oxygen processing equipment. Air separation units and/or oxygen tanks are required to supply additional oxygen to these systems. There is also the issue of increased wear on combustor components. Increased oxygen content means higher temperatures, more thermal cycling from thermally induced stress, and the potential for shorter useful life. This shortening of component life can also be exacerbated by oxygen embrittlement of the metallic parts. Figure 2 illustrates cracks that formed in a heat exchanger tube and tube sheet due to thermal fatigue.

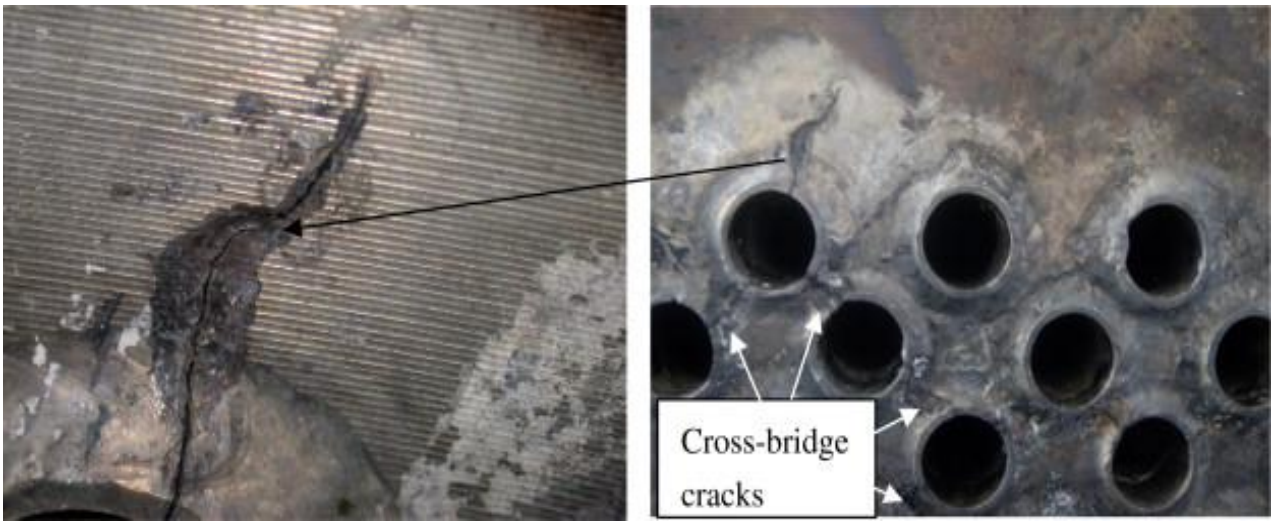

Figure 2: Thermal Fatigue Cracks Formed in a Heat Exchanger Tube Sheet [8]

1.2 Diagnostic Methods Used in Soot and Flame Characterization

There are a multitude of ways that soot formation is studied in oxygen combustion. In the early days, with a lack of today's modern measuring equipment, tools as simple as rulers were used to quantify soot formation. As previously discussed, Saito et al. [9] used the measurement of various flame region heights and the deposition of soot onto a quartz filament to attempt to answer the question of how small additions of oxygen to the fuel stream of a diffusion flame affected the soot formation. Today, however, we have more advanced techniques to be able to probe deeper into the heart of the issue of soot in flames. Some of these techniques include thermophoretic sampling and subsequent TEM (Transmission Electron Microscopy), flame temperature measurements, fringe analysis, laser light extinction, atomic force microscopy, and computational techniques. This work primarily focuses on the first four techniques, but others will be discussed due to their use in preexisting literature.

1.2.1 Thermophoretic Sampling and TEM Analysis

Thermophoretic Sampling

The next technique researchers utilize to study soot is thermophoretic sampling. This method utilizes temperature differentials between a hot gas and a colder sampling apparatus to "freeze" particles within the gas stream to the sampling apparatus. These particles can then be analyzed in a multitude of ways, SEM and TEM, but the method of focus here is through TEM analysis. This will be discussed in more detail later in subsequent sections. Thermophoretic sampling has the benefit of allowing researchers the ability to sample delicate flame-generated structures. However, due to the delicate nature of some phenomena of sampling interest (i.e., co-flow flames), parameters such as residence time must be carefully tailored to ensure accurate nanoparticle representation in the sample. There also must be a strong temperature gradient for the sampled particles to be able to "freeze" to the sampling apparatus's substrate [10].

TEM Grids

The sampling apparatus for thermophoretic sampling can take a myriad of forms. In the case of this work, it takes the form of a TEM grid. This grid is metal and is a flat disk filled with regularly spaced holes. The metal for this disk is chosen based on desired properties such as corrosion resistance. There is then a layer of carbon added to one side of the disk on top of the disk mesh, known as the C-film. The carbon layer can either be solid or what is known as "lacey" or "holey" grids. These non-solid carbon layers serve the purpose of increasing image contrast and eliminating any image distortion from imaging the carbon layer as well. Magnified images of the different carbon layer types can be seen in Figure 4, and images of the TEM grid setup types can be seen in Figure 5. This layer is typically between 3-30 nm thick, depending on the needed electron transparency and substrate strength [11]. This layer must be thin enough for electrons to pass through, as they also pass through the samples during TEM analysis.

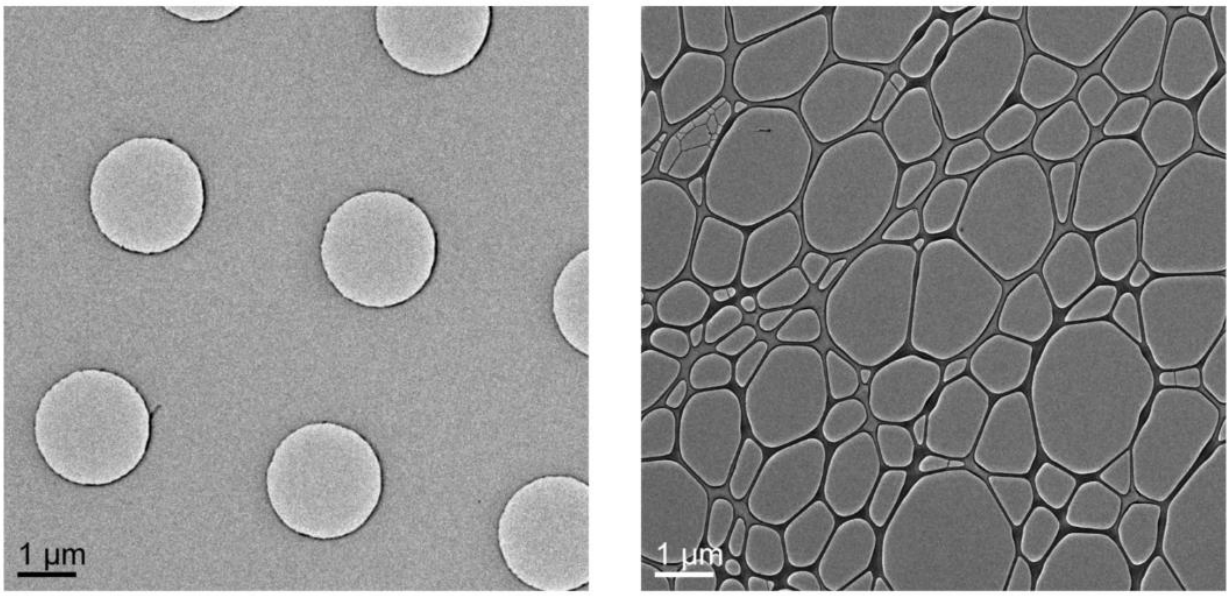

Figure 3: Holey and Lacey Carbon Substrates for TEM Grids [12]

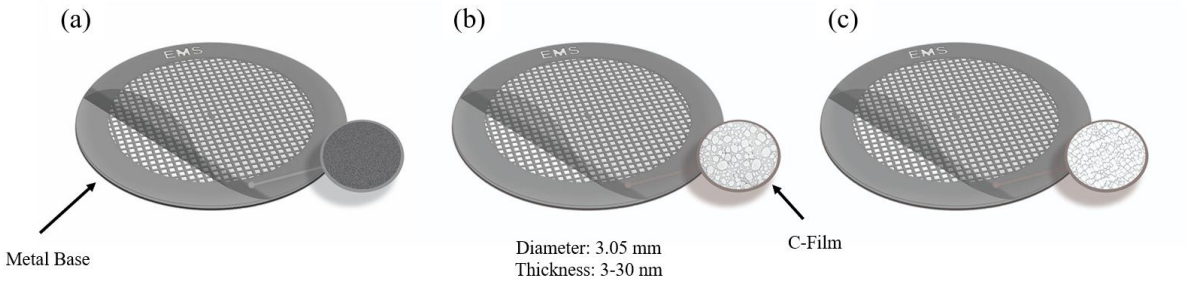

Figure 4: Typical TEM Grid Layer Types [13]

In instance of collecting soot samples. The TEM grids must be inserted into the flame and are typically actuated by either a hydraulic or pneumatic cylinder. Once the grid is inside, the flame is then held there for a predetermined amount of time and then taken out. The amount of time the grid spends in the flame is known as residence time and must be long enough for the flame's flow state to recover from the probe being inserted, but short enough as not to burn the grid's carbon coating. It should also be noted that the actual travel time for the grid both into and out of

the flame should be kept to a minimum. This is done to reduce sampling contamination from picking up particles from flame regions that are not of interest, especially if trying to sample the flame's core. A schematic of a thermophoretic sampling process using a TEM grid is visualized in Figure 6.

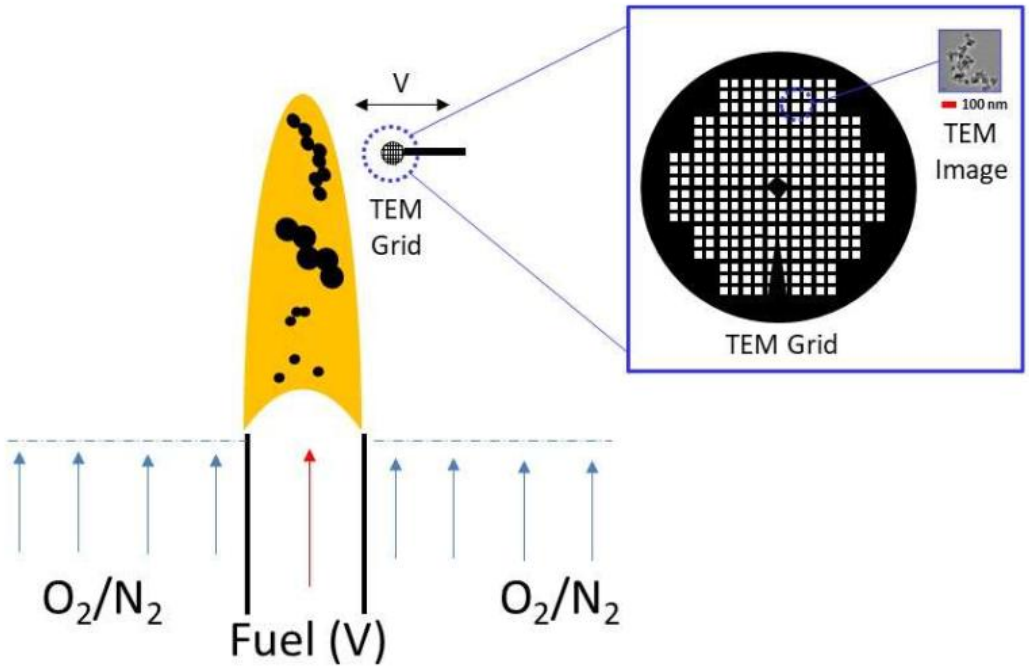

Figure 5: Thermophoretic Sampling Using a TEM Grid in a Co-Flow Diffusion Flame [14]

Once the soot samples are collected, they need to be analyzed. One way this is done is with TEM analysis. TEM works by passing a beam of electrons through a thin sample. Some of these electron paths are altered by interactions with the internal structure of the sample, while some are not. The electron beam is then focused onto detectors where a high-detail image of the sample's internal structure is produced. Due to soot particles typically being on the order of 100 nm in diameter [14], TEM can be utilized for their study. In soot studies, TEM can be used to find quantitative metrics on the soot's morphology. Metrics such as average soot primary particle diameter, and degree of agglomeration can be measured, but also more internal metrics such as tortuosity (ratio of layer fringe path lengths to Euclidean distance between fringe endpoints), circularity, and layer stacking.

TEM for Soot Characterization

For this work, TEM analysis is used to analyze soot morphology. This means looking at soot particles at various magnifications. Lower magnifications are used to analyze the overall soot population density. Medium magnifications are used to determine metrics like primary particle diameter. Lastly, high magnifications are used to probe the inner structure of soot particles. Figure 6 shows soot particles/aggregates are various magnifications.

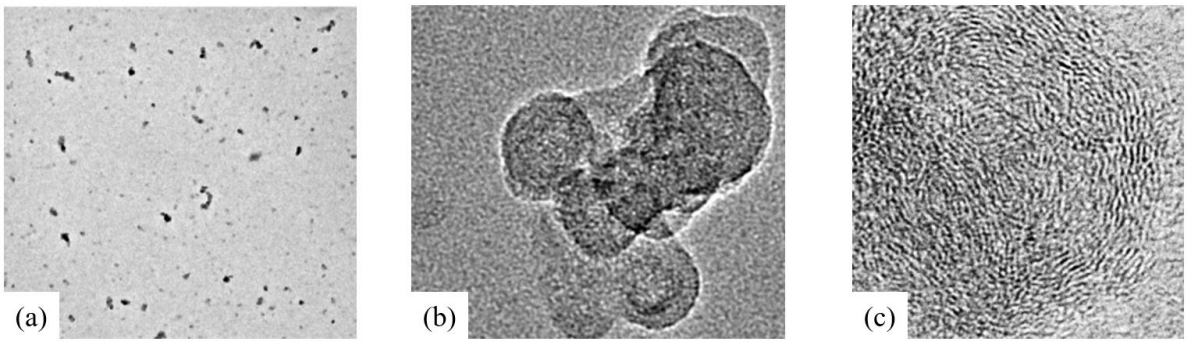

Figure 6: TEM Images of Soot at Various Magnifications

In the figure, Figure 6 (a), 6 (b), and 6 (c) represent low, medium, and high-resolution TEM images of soot. Quantities like soot primary particle diameter and degree of agglomeration can be taken from low and medium magnification images, but to see the soot's internal structure, high-resolution images must be used. In Figure 6 (c), this internal structure is visible. This structure is of interest to the present work. This structure will be analyzed using image processing software in a later section.

1.2.2 Flame Temperature Measurements

Thermocouples

Another important metric for researchers interested in soot production in flames is flame temperature. It is well known that with increased temperature, chemical reaction rates also increase. These temperature measurements can be taken in a variety of ways. Direct methods, such as thermocouple measurements, and optical methods, such as pyrometry or spectroscopy, are commonly used. In the context of this work, direct measurements using a thermocouple will be utilized, but optical methods will be discussed. The use of thermocouples in this work is due to the relatively inexpensive nature of "low" response time thermocouples (able to be used due to the relative temporal stability of laminar flames). Thermocouples work using the Seebeck effect, which states that an induced voltage will occur in the junction between two dissimilar metals when said junction is exposed to a temperature gradient [15]. This induced voltage can then be read by a DAQ (data acquisition) system and converted to a corresponding temperature. A schematic of the general setup of a thermocouple can be seen in Figure 7.

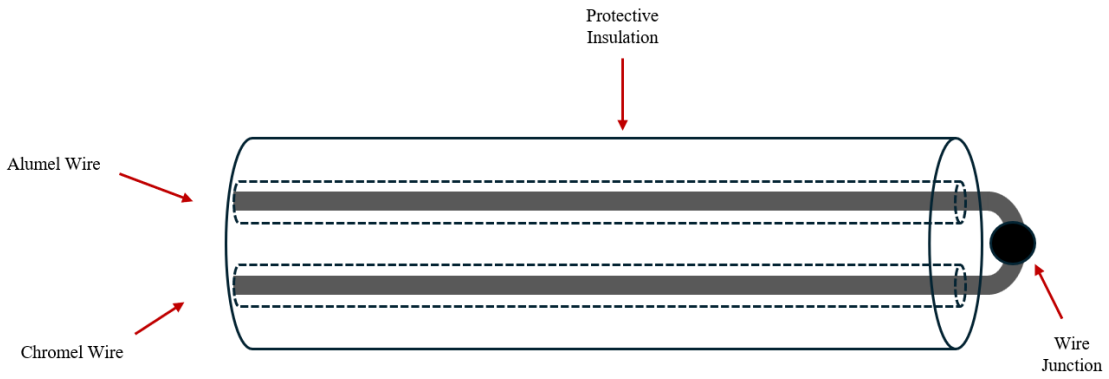

Figure 7: Schematic of a Type K Thermocouple

Special care must be taken when selecting a thermocouple for flame temperature measurement. There is one aspect to consider. Depending on fuel/oxidizer types, flames can reach temperatures of 2000+ Kelvin [7]. Different types of thermocouples are made of different metals, meaning different melting temperatures. The types also have operating temperature ranges, typically

where their temperature-to-voltage response is predictable. Another aspect that should be considered for thermocouple selection is their size. This must be considered as a large thermocouple would noticeably perturb the flame, making the commonly used assumption that the thermocouple is a non-dimensional point invalid.

Optical Pyrometry

As mentioned in a previous section, optical techniques will also be discussed, as they are used extensively in literature for flame temperature measurements. While not utilized in this work, an understanding of optical temperature measurement techniques is important to broaden the understanding of various ways that temperature is measured in flames. One such technique is known as optical pyrometry. Optical pyrometry is a non-intrusive method that relies on Planck's law to determine the temperature of an observed object. The law states that the spectral radiance (the energy a body radiates at different frequencies) of an object depends on the temperature of the object and the wavelength of the radiation emitted by said object. Equation 3 shows this law.

$$B_\lambda(\lambda, T) = \frac{2hc^2}{5} * \frac{1}{e^{\frac{hc}{\lambda k_B T}} - 1} \tag{3}$$

Where $B_\lambda(\lambda, T)$ is the spectral radiance of the object in question as a function of its wavelength (λ) and temperature in Kelvin (T), h is Planck's constant, c is the speed of light in the medium of question, and k_B is the Boltzmann constant. As a result of this equation, the spectral radiance is a function of wavelength and temperature [16]. Optical pyrometry uses this fact by measuring the radiation emitted by an object at a set wavelength(s), and then solving the above equation for the temperature, leading to an estimation of the temperature of the object in question.

Pyrometers that use a single wavelength are known as monochromatic pyrometers. One type of monochromatic pyrometer is the disappearing wire pyrometer. This device uses a heated filament that will be incandescent at different wavelengths depending on the user's-controlled

current [17]. The color of this filament can then be matched to that of the target object to obtain a temperature. Figure 8 shows a schematic of this process.

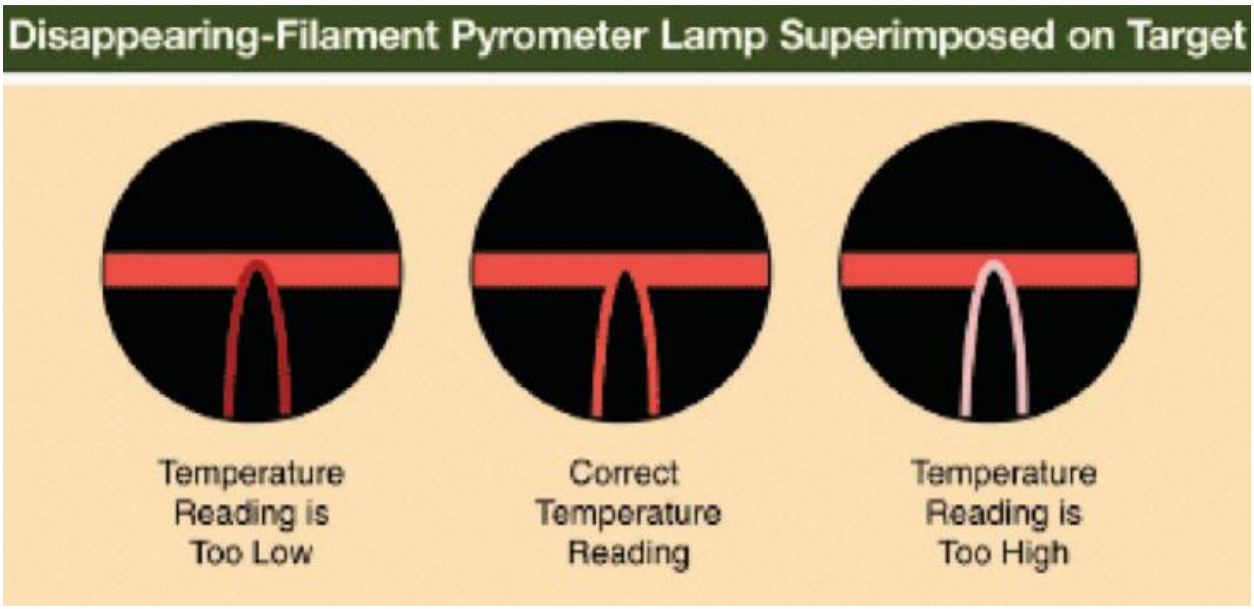

Figure 8: Schematic of Disappearing-Filament Pyrometry Color Match [18]

As seen in the figure above, the color of the pyrometer's filament is changed until it matches that of the target, and then the equipment uses Planck's equation to estimate the temperature of the target.

Unlike thermocouples, optical pyrometry comes with the benefit of being a non-intrusive technique. The pyrometer's filament does not have to be inserted into the flame like a thermocouple does, meaning that the flame is not perturbed by the measurement. Pyrometry also comes with the benefit of being able to measure higher temperatures than most thermocouples, since there is not a risk of the measurement device melting in the flames. This temperature measurement technique does come with the downside of potential temperature errors. These errors can be introduced because emissivity is assumed to be constant as the target object is assumed to behave as a blackbody, and real surfaces do not behave as black bodies due to surface roughness, viewing angle, etc.

Considering this techniques' benefits, optical pyrometry or other optical techniques would be ideal for measuring temperatures in oxygen-enriched flames, due to the harsher environments. Optical techniques were not used in this work; however, their use is suggested for use in oxygen-enriched flames in the “Future Works Recommendations” section.

1.2.3 Laser Light Extinction

A schematic of this technique can be seen in Figure 9. At its core, this method revolves around laser light. In this example, a Helium-Neon laser is passed through a medium that contains particulate matter. Some of the light is absorbed by the medium, some is scattered by either medium particles or the particulate matter to be measured, and some is reflected or diffracted. These mechanisms all act to lower the intensity of the light beam. The laser light then arrives at some kind of photo detector/power meter, where its intensity is measured. This intensity is then compared to the original unaltered intensity to determine the extinction coefficient of the medium, and then the particle number density. For soot studies, this method is typically used to take soot volume fraction measurements. This metric provides the proportion of the medium volume that is occupied by particulate matter (in this case, soot). This allows researchers to assess the amount of soot present in a flame and gauge the effectiveness of their control methods.

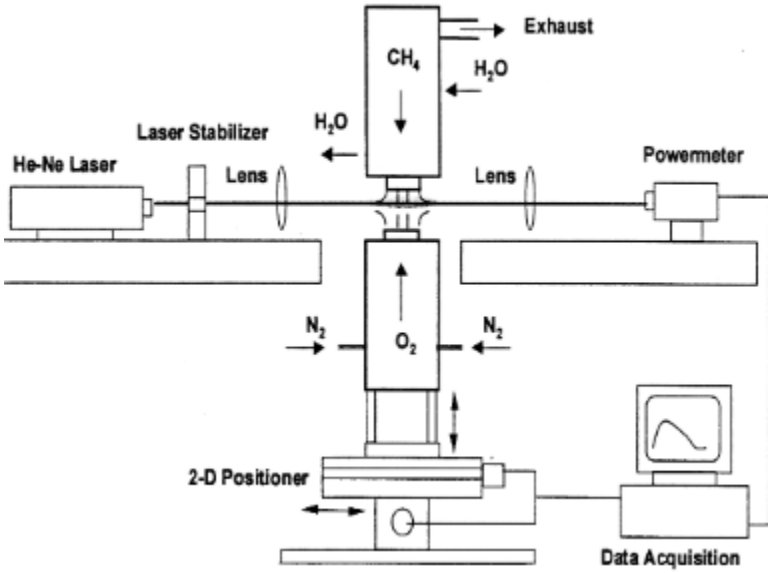

Figure 9: Laser Light Extinction Schematic [19]

Chapter 2: Soot Formation in Flames

2.1 Formation and Evolution

Soot formation in flames is a complex process. It depends on a multitude of factors such as flame residence time, chemical makeup of fuel, oxidizer used, combustor geometry, flame temperature, etc. This makes it exceptionally difficult to determine the sooting characteristics of real-world combustion systems, as they include these factors and other complexities such as turbulence. Because of this, researchers use simplified flames to be able to study soot formation pathways. One common type of flame that is used for this purpose is the laminar diffusion flame. Laminar diffusion flames are flames which the mixing of the fuel and oxidizer only occurs through diffusion when they meet at the flame front. Due to this, the flame will be very structured, have well-defined regions, and lack turbulence [2]. Soot formations in these flames have well-agreed-upon phases, though some argue various phases should be grouped or separated. For this work, six distinct phases will be considered for completeness of understanding. The list below contains these phases.

I. Hydrocarbon Fuel Decomposition
II. Formation of Soot Precursors
III. Particle Inception (Nucleation)
IV. Particle Surface/Mass Growth
V. Particle Aggregation
VI. Oxidation

A visualization of this process can be seen in Figure 10. The first step in the soot formation process is the pyrolysis of the fuel. Due to the high temperatures of combustion, hydrocarbon fuels undergo thermal decomposition into lower-level constituents. Some examples include methyl (CH_3) and acetylene (C_2H_2). These constituents begin to form aromatic rings, which are cyclic, planar molecules such as benzene (C_6H_6). These aromatic rings then begin to combine to form PAH's (polycyclic aromatic hydrocarbons). These PAH molecules are in gaseous form, where they are known as soot precursors. These molecules will continue to grow through

nucleation as they capture other atoms/molecules. They will eventually condense as they grow due to various factors such as flame location (and by virtue of temperature), PAH molecule size, etc. Once these masses reach a critical size of 3,000-10,000 atomic mass units, they are then identified as individual particles. As these particles travel up through the fuel-rich regions of the flame, surface mass growth occurs. Soot particle surface radicals react with the constituents of the initial fuel pyrolysis to deposit carbon atoms. As the soot particles grow, they also collide and attach, either mechanically or chemically. If mechanical, the process is typically known as agglomeration, as the individual molecules are loosely bonded by mechanical bonds. If the particles chemically bond, it is known as an aggregation, as they are bound by stronger forces. These terms for this process are often used interchangeably in soot studies for simplicity. Either way, this process produces larger branch-like structures that can be seen towards the top of the flame in Figure 10. Soot growth is counteracted by oxidative attack on aggregates. Carbon atoms are removed from the surface of aggregates/soot particles by reacting with O_2, O, and OH radicals (the most reactive), and become CO and CO_2. This can shrink the particles or break up aggregates by dissolving their loose mechanical bonds. These processes compete throughout the flame. Soot growth dominates in fuel-laden parts of the flame, whereas oxidation reigns in oxygen-rich regions. Towards the top of the flame, oxidation is dominant due to oxygen's availability. If the soot's residence time within the flame is long enough, it will have ample time to be oxidized completely into CO and CO_2. If not, soot particles will escape from the flame tip. This is known as a sooting flame.

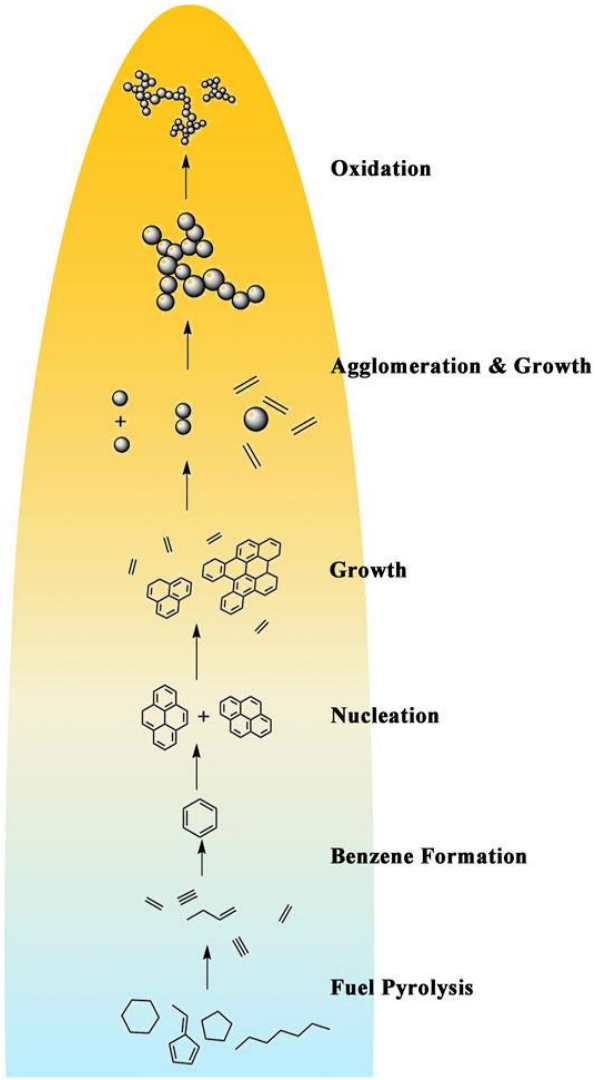

Figure 10: Soot formation in flames [20]

2.2 Soot Flame Studies

2.2.1 Co-Flow Diffusion

Introduction of Oxygen to the Oxidizer

In combustion, there are multiple ways that additional oxygen can be introduced to the system. This section will focus on a common method: introducing additional oxygen into the oxidizer stream. A schematic of a typical oxy-combustion burner can be seen in Figure 11.

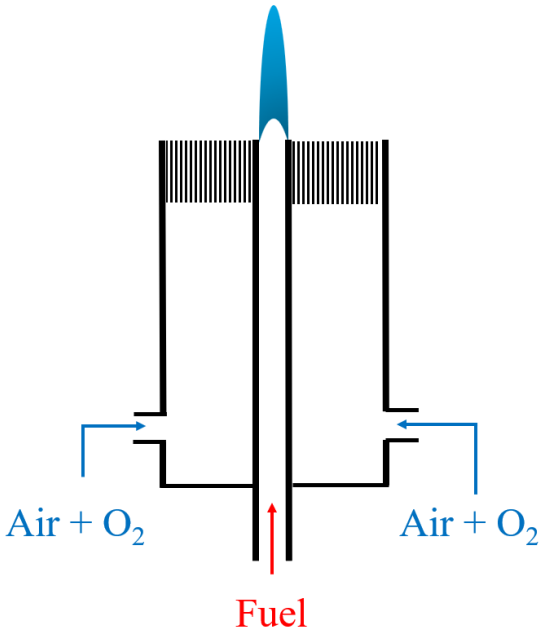

Figure 11: Typical Burner Configuration for Oxygen to be Added to the Oxidizer Stream of a Co-Flow Burner

Various works have investigated the effect of adding oxygen to the oxidizer stream in co-flow flames. Table 1 contains a summary of the literature on soot investigations in co-flow laminar diffusion flames. It contains information on the authors, fuel, oxidizer, and experimental techniques used, as well as schematics of the burner configuration for each study.

Table 1. Summation Table for Soot Studies Using Co-Flow Laminar Diffusion Flames

Author	Fuel	Oxidizer	Techniques	Burner Configuration
Co-Flow Laminar Diffusion: Oxygen Added to Oxidizer				
Lee et al.	Methane	Air + O_2 (21%, 50%, 100%)	Thermophoretic Sampling (Dp, nm) (Soot volume fraction, ppm)	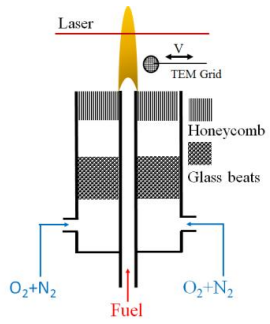
Zelepouga et al.	Methane + PAH Doping	Air + O_2 (21%, 35%, 50%, and 100%)	Soot volume fraction	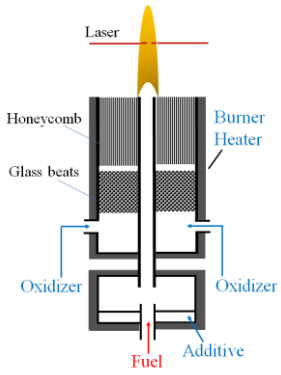
Merchan-Merchan et al.	Biodiesels: B100CME and B100SME	Air + O_2 (21%, 35%, 50%, and 100%)	Soot volume fraction	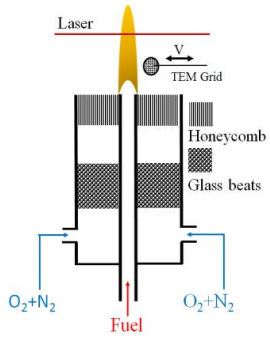

Deal et al.	Biodiesels B100CME and No.2 Diesel	Air + O_2 (21%, 35%, 50%, and 80%)	Primary Particle Diameter	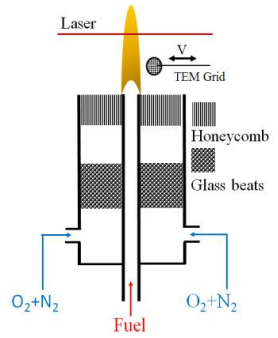
Co-Flow Laminar Diffusion: Oxygen Added to the Fuel				
Saito et al.	Methane O_2: 1.14%, 2.09%, and 3.08%	Air	Flame region height measurements/chemical compositions	No schematic as burner diameter varied.
Gulder	Methane, Propane, n-Butane with oxygen mole fractions ranging from 0-0.16	Air	Soot volume fraction/ Flame profiles	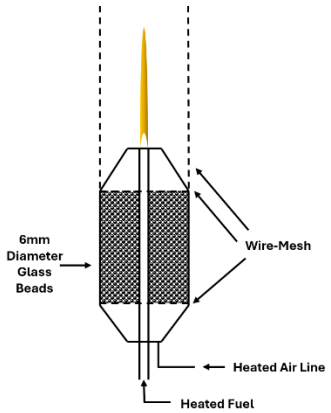

Merchan-Merchan et al. (Merchan-Breur)	Biodiesels: CME, COME, SME Diesel: No.2	Air + O_2 (21%, 35%, 50%, 80%)	Thermophoretic sampling, TEM analysis	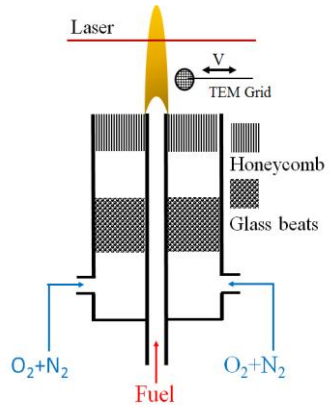

Lee et al. [21] investigated how soot formation is changed by the addition of various oxygen concentrations in the oxidizer stream of a non-premixed, laminar methane flame. They investigated three experimental flames. These experimental flames were methane, burned with 50% N2-50% oxygen as the oxidizer, methane burned with 100% oxygen as the oxidizer, and methane burned with air (21% oxygen) as the oxidizer. The researchers employed thermophoretic sampling and TEM analysis to investigate soot structure, and laser-light extinction to measure the soot volume fractions of both the control and experimental flames at various axial distances. They found that for the air and 50% oxygen flames, the soot primary particle size was not noticeably changed, but it was lower by a factor of two for the pure oxygen flame. They also found that with increased oxygen content, soot inception rates grew.

Like the work just discussed, Zelepouga et al. [22] also investigated soot evolution in co-flow methane flames with both air and enriched air as the oxidizer. However, their primary goal was not to investigate the effect of the enriched air on the soot evolution of these flames, but to investigate the effect of the addition of small quantities of acetylene and PAHs (polycyclic aromatic hydrocarbons) on soot formation. They used four reference flames with oxygen contents of 21, 35, 50, and 100 % in the oxidizer stream. The four main additives they were testing were acetylene, phenanthrene, pyrene, and acenaphthene. They found that all additives significantly increased soot formation in reference flames, and that the PAH additions' effect

became substantially stronger with increased oxygen content. Methane and other simple hydrocarbons are not the only pertinent fuels in the study of soot formation in oxygen-enhanced flames. Alternate fuels such as biodiesel are also of interest. Merchan-Merchan et al. [23] investigated soot formation in co-flow diffusion flames with oxygen-enhanced air. For this experiment, they utilized two FAME (fatty acid methyl esters) biodiesels, neat canola methyl ester (B100CME) and neat soy methyl ester (B100SME), and had 4 test conditions varying the oxygen content in the oxidizer stream. These conditions were 21, 35, 50, and 80% oxygen. Laser light extinction was used to quantify soot formation through the measurement of soot volume fractions. It was found that when oxygen content is raised, initially, soot formation is promoted, but then is suppressed if the oxygen content is increased further. The authors hypothesize that the eventual soot formation reduction is due to temperature effects. When more oxygen is added, the flame burns hotter and has a smaller volume, both increasing fuel pyrolysis. This increase of fuel pyrolysis leads to a reduction in soot precursors being available, and in turn reduces the overall sooting propensity of these flames.

Introduction of Oxygen to the Fuel

Another way additional oxygen can be added to a combustor is through its addition to the fuel. This oxygen can be added either by adding it to the fuel stream or by utilizing fuels that contain oxygen in their chemical structures. Figure 12 illustrates the typical burner configuration when oxygen is added to the fuel stream, typically in gaseous form. This condition has been the topic of interest since the 1980s. Saito et al. [24] in 1984 wanted to explore the effect of small quantities of oxygen being added to the fuel stream of a methane/air diffusion flame on the sooting tendencies of said flame. Although a quasi-open-air methane flame (a wire mesh was used for flame stability) was utilized in this study, it should be no different from a co-flow diffusion flame using air for the oxidizer steam. They had 4 conditions, pure methane, methane + 1.14 % O2, methane + 2.19 % O2, and methane + 3.08 % O2 all on a molar basis. These percentages were chosen due to a previous study conducting similar research at 10-20%. These researchers used measurements of the flames' sooting height, a quantity they denote as h3, and gas chromatograph species composition to quantify the sooting propensity of the flames. They found that there were minimal changes to the flame sooting height. They also discovered that

there was no influence on the stable species concentrations regardless of added oxygen content. This led to the conclusion that, at least in small concentrations, additional oxygen added to the fuel stream has a minimal effect on soot production in methane diffusion flames.

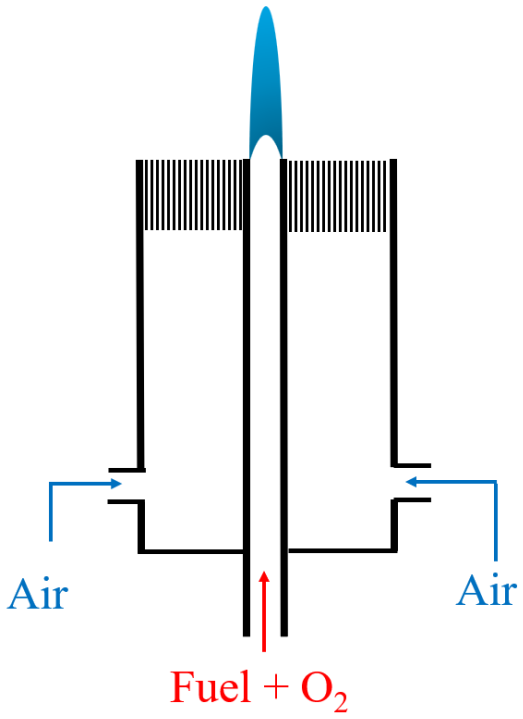

Figure 12: Typical Burner Configuration for Oxygen to be Added to the Fuel Stream of a Co-Flow Burner

Since the maximum mole fraction of oxygen in the fuel/oxygen mixture was 0.045 in the work of Saito et al., questions were raised about the validity of their conclusions, due to the low concentrations of oxygen present in the fuel stream. To attempt to rectify this gap, Gulder et al. [25] performed a study of the effects of the sooting propensity of diffusion methane flames at higher oxygen mole fractions, as high as 0.16. They also investigated the same effects on propane and n-butane flames. The researchers used laser light extinction to measure soot volume fractions. When the influence of temperature and dilution were considered, it was found that the addition of oxygen chemically suppresses soot formation in methane flames. This was argued to be due to the reduction of acetylene, an intermediate in the pyrolysis of methane. The opposite trend was found, however, for propane and n-butane, where increased oxygen volume fractions in the fuel stream enhance soot formation.

The second way to add oxygen to the fuel is through its chemical makeup. Biofuels are used for this since they are derived from organic matter, and they typically contain oxygen in the chemical structure of the fuel. Examples of such fuels include biodiesel canola methyl ester ($C_{19}H_{36}O_2$) or ethanol (CH_3CH_2OH). Equations 4 and 5 show the combustion of canola methyl ester and ethanol with air, respectively.

$$C_{19}H_{36}O_2 + 27(O_2 + 3.76N_2) \rightarrow 19CO_2 + 18H_2O + 101.52N_2 \quad (4)$$

$$CH_3CH_2OH + 3(O_2 + 3.76N_2) \rightarrow 2CO_2 + 3H_2O + 11.28N_2 \quad (5)$$

As can be seen in these chemical formulas, both canola methyl ester and ethanol contain hydrogen and carbon atoms (much like traditional hydrocarbons), but they also contain oxygen atoms. The effect of this atomically bonded oxygen is the topic of research performed by Deal et al. [26]. They investigated the effect of the atomically bonded oxygen in CME (canola methyl ester) on this fuel's sooting properties and compared it to that of a more traditional fuel, No. 2 Diesel. Both fuels were burned with varying oxygen content in the oxidizer stream, specifically 21% (air), 35%, 50%, and 80%. While the presence of additional oxygen in the oxidizer stream is present, the main topic of this work was to analyze how the oxygen in the fuel would affect its sooting properties, which is the reason this work is discussed in the "introduction of oxygen to the fuel" section of this work. It should also be pointed out that the authors did not utilize the 100% oxygen condition, due to the relatively small flame sizes and elevated temperatures. For this study, the authors used thermophoretic sampling and TEM imaging to measure soot primary particle diameter (dp). This metric was used to quantify the sooting propensity of these flames. It was found that the CME flames did not have soot growth regions above their luminous zones as do the No. 2 diesel flames. For both flames, as oxygen content increased, peak dp began to increase but then sharply decreased. This is consistent with the words previously discussed, as they found a similar trend in the soot volume fraction measurements with increased oxygen content in the oxidizer stream. The researchers also found that the peak dp was always higher for the No. 2 diesel flames than that of the CME flames, regardless of oxidizer stream oxygen content. Both the lack and a soot growth zone in the CME flames and the lower peak dp value,

regardless of oxygen content, corroborate the claim that the atomically bonded oxygen in the CME has a negating effect on soot growth.

2.2.2 Premixed Flames

The discussion of flames thus far has been centered around non-premixed, laminar diffusion flames. Though other flame types are not the topic of this work, it is important to understand a variety of flames due to their varying structure and thereby varying sooting properties. This information is important as it shows why co-flow non-premixed flames were chosen. Table 2 contains a summary of literature pertaining to soot investigations in two additional flame types: premixed co-flow diffusion and counterflow flames. It contains information on the authors, fuel, oxidizer, and experimental techniques used, as well as schematics of the burner configuration for each study.

Table 2. Summation Table for Soot Studies of Premixed Co-Flow Diffusion Flames and Counter-Flow Diffusion Flames

Authors	Fuel	Oxidizer	Techniques	Burner Configuration
Premixed				
Harris and Weiner	Toluene/Ethylene Mixture	Air Equivalence Ratios: 1.78-1.92	Soot volume fraction	Water-cooled porous plug burner
Ramer et al.	Methane	O_2 Equivalence Ratios: 1.09,1.22, and 1.41	Soot volume fractions, gas chromatograph, photon correlation spectroscopy	6 cm diameter flat-flame burner (McKenna Products)
Counterflow				
Beltram et al.	Methane	Air + O2 (21%-100%)	Soot volume fraction	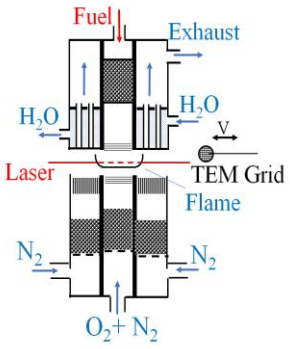

Premixed flames are the first additional flame type to be discussed. This flame type is very similar to non-premixed laminar diffusion co-flow flames, with the exception that the fuel and oxidizer are mixed before reaching the reactor. This results in a different flame structure than that of non-premixed flames. Figure 13 illustrates this flame structure.

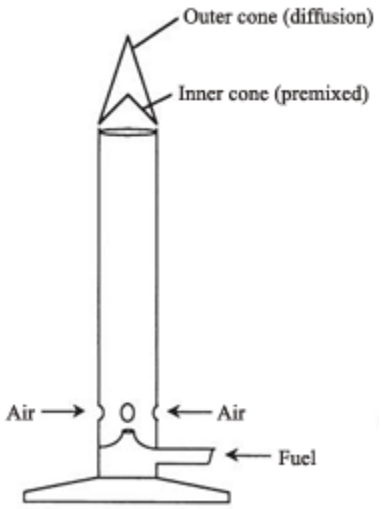

Figure 13: Flame structure of Bunsen Burner Style Premixed Flame [2]

Since diffusion is not the main mode of mixing in these flames, they do not showcase the equivalence ratio-dependent zones that are present in non-premixed flames. As can be seen in the above figure, the annular regions are absent. Instead, a cone or dome-shaped primary flame can be seen close to the burner mouth, and a second outer diffusion flame surrounds the first. Soot formation in premixed flames is governed by the same chemical kinetics as non-premixed flames and is highly dependent on equivalence ratio (only forming in regions where $\varphi > 1$). This means that premixed flames are, by nature, less sooty than non-premixed flames and only produce soot when running fuel-rich. This also means that there is no good way to define "oxygen enhanced" for premixed flames. Instead of adding oxygen to the oxidizer stream as with non-premixed, it is already incorporated into the premixed fuel/oxidizer stream, so the equivalence ratio is typically the parameter used to keep track of oxygen content.

It is well agreed upon in the literature that soot formation in premixed flames consists of two steps, inception and surface growth. This surface growth rate is the driving factor behind soot formation and is the topic of much of the literature on premixed flames. One of the first studies into acetylene's role in premixed flame soot formation was that of the work of Harris and Weiner [27]. They investigated soot particle growth in premixed toluene/ethylene flames using ultimate soot volume fraction measurements. These measurements were then used to calculate the soot particle growth rates. They varied the C/O ratio (carbon/oxygen ratio in the fuel) by changing the

mixture of toluene/ethylene, with values of the C/O ratio ranging from 0.637 to 0.693. Most of the carbon was supplied by the toluene. The investigators also varied the equivalence ratio from 1.78 to 1.92. The researchers found that the soot surface growth rate is relatively unchanged by varying the fuel mixture. They also found that toluene/ethylene flames produce more soot overall than ethylene flames at a given C/O ratio, with most of the carbon coming from acetylene. This led the researchers to conclude that the particle inception stage controls the overall amount of soot produced. They speculate this is due to this stage determining the surface area available for growth.

Later, Ramer et al. investigated soot formation in methane/oxygen flames. They used a flat flame burner that utilized a nitrogen sheath to isolate the flame from the surrounding atmosphere. The researchers varied fuel/oxidizer ratio, with the investigated ratios being 1.09, 1.22, and 1.41. They collected and analyzed gas samples using a quartz probe and a gas chromatograph, respectively. This was done to determine the present mole fractions of primary products in the burned gas (hydrogen, oxygen, carbon dioxide, C_1, C_2), with C_1 and C_2 designating hydrocarbons that contain one and two carbon atoms, respectively. They also measured soot number density, soot volume fraction, and soot particle size using various optical techniques. Soot particle surface area was calculated from measured quantities of most probable size, geometric standard deviation, and number density. It was found that in all flames surveyed, a soot mass increase was accompanied by an increase in the loss rate of acetylene. This led the investigators to assume the acetylene was the primary source of the growth carbon needed for the soot surface growth [28]. This conclusion agrees with the previous work of Harris and Weiner, discussed above.

2.2.3 Counter-Flow Flames

Other than co-flow flames, there is another type known as counterflow. From the name, the nature of these flames can be inferred, i.e., they consist of fuel and oxidizer streams directly

impinging on one another, creating a flat flame between them. Figure 14 shows a schematic of a typical counter-flow reactor setup and a resultant flame.

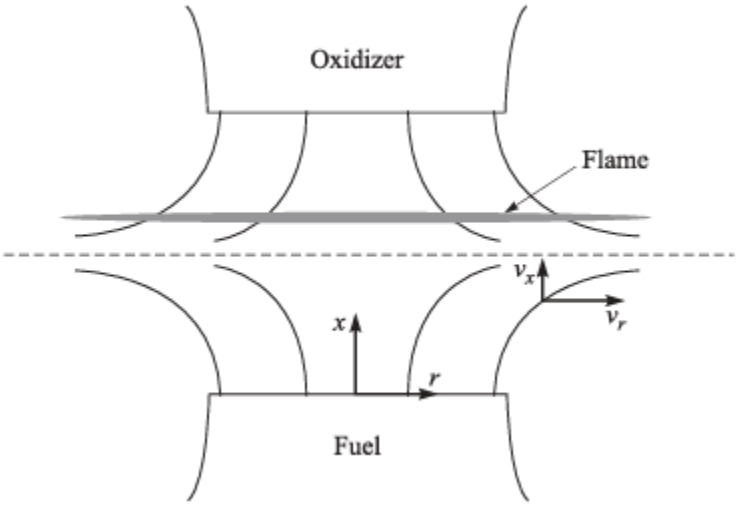

Figure 14: Schematic of Typical Counterflow Diffusion Flame Reactor Setup [2]

In the figure, the axes are defined with x being the axial direction and r being radial. Accordingly, v_x and v_r are the flow velocities in the axial and radial directions, respectively. Since the fuel and oxidizer streams both point towards one another, a stagnation plane (axial location where the fluid momentum velocities are equal) is formed. A flame sheet is generated where the fuel and oxidizer meet from diffusion across the stagnation plane. The sheet forms slightly on the oxidizer side of the stagnation plane. This flame sheet is very thin and can be approximated as a 1-D flame. Because of this and the fact that diffusion governs the dispersion of the two reactant streams, counter-flow flames can be used to approximate the conditions found in the flame front of co-flow flames. This is useful to researchers as it allows them to decouple the chemical kinetics and transport phenomenon.

One study that has been conducted to investigate soot formation in oxygen-enhanced counter-flow flames is the work of Beltrame et al. They investigated both soot and NO_x formation in

methane-oxygen enriched counterflow diffusion flames [29]. The investigators conducted multiple experiments, but one of the interests of this work is their experiment involving soot volume fraction measurements. They took these measurements from methane flames with oxygen content varying from 21%-100%. They found that generally, with an increase in oxygen content, soot formation is enhanced. This is consistent with the sooting behavior of the previously mentioned flame types. Soot inception is increased with an increase in oxygen content. This study does not capture the decrease in net overall soot output due to increased oxidative attack. This is because, due to the 1D nature of counterflow diffusion flames, there is no residence time for the soot in oxygen-rich zones, meaning it does not undergo this oxidative attack.

2.3 Motivation/Thesis Objective

In this work, soot morphology and nanostructure will be investigated for methane non-premixed laminar flames using 100% oxygen as an oxidizer. A similar flame burning methane and air (21% oxygen) will be used for comparison. This topic was chosen due to a lack in the literature of a study that utilized more than 80% oxidizer, due to temperature and flame height challenges. There is also a lack in the literature on the oxygen-enriched environment's effect on the nanostructure of soot particles, and its change with temperature. In summary, the objectives of this thesis are:

1. Present the soot particle diameter and general morphology of soot aggregates along the axial direction of a 100% oxygen methane flame using low and medium magnification TEM image analysis.
2. Present the nanostructure of soot trapped along the axial direction of the 100% oxygen methane flame using high resolution TEM images.
3. Compare soot from 100% oxygen methane flame, including soot particle diameter, nanostructure, and evolution, to soot from a 21% oxygen methane flame.
4. Correlate axial flame temperatures with soot evolution, diameter, and nanostructure

Chapter 3: Experimental Approach

The methods/equipment used for the experiments will be presented in this chapter. The choice of methane as the fuel of interest will also be discussed. The setup for the experiments conducted for this work contains that of a co-flow burner, thermophoretic sampler utilizing TEM grids with motion control system, an electron microscope for analysis, and thermocouples for flame temperature measurements. Figure 15 shows a schematic of the overall experimental setup.

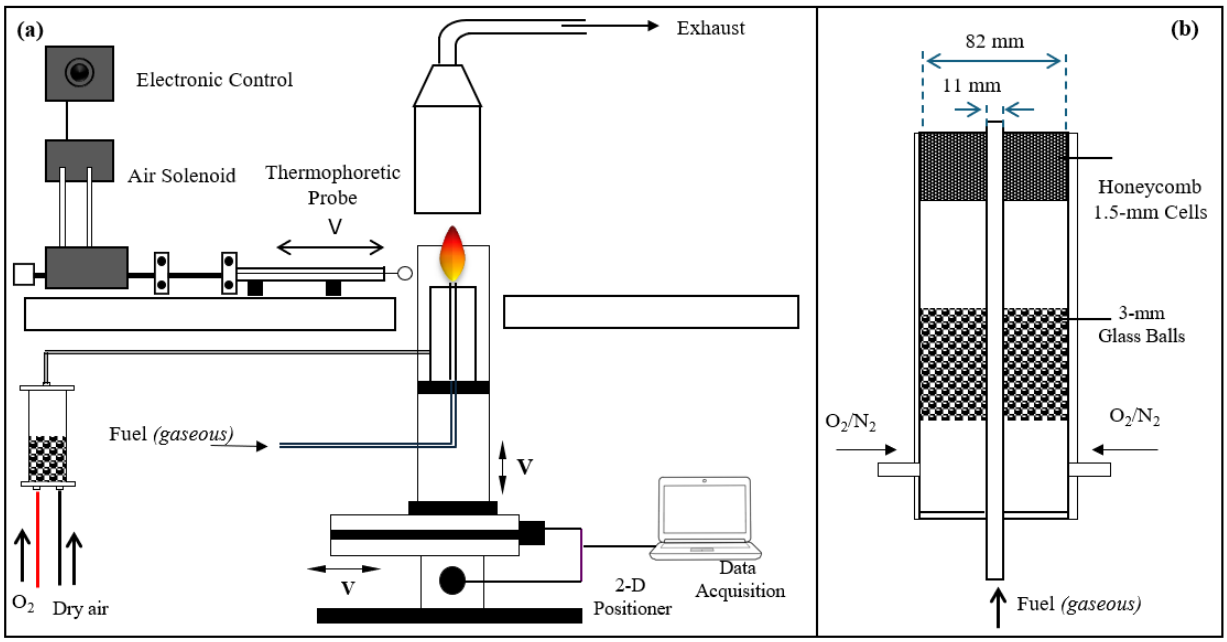

Figure 15: (a) Schematic of the Experimental Setup Used to Study Soot Formation Using Thermophoretic Sampling Technique from Methane/Air and Methane/Oxygen Flames; (b) Detailed View of the Co-Flow Burner

Figure 15 (a) presents a schematic of the overall experiment setup including the thermophoretic sampling system, fuel delivery system and oxidizer delivery system. Figure 15 (b) presents a detailed view of the burner used. More details on this equipment and methods used can be found in the following chapter.

3.1 Burner Configuration

The burner used for this work is based off the co-flow burner used by Santoro et al. [30]. The schematic of this burner can be seen in Figure 16.

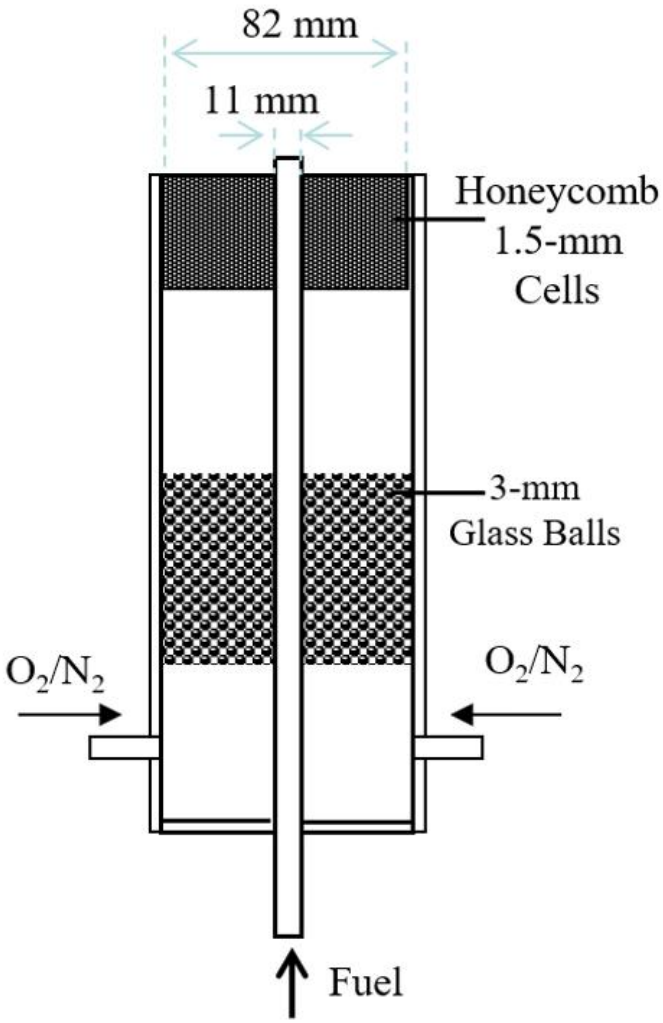

Figure 16: Schematic of Co-Flow Burner Used for Experiments

As seen in the figure, that co-flow burner consists of two concentric tubes of diameter 82 mm and 11mm respectively. The entire burner is 178 mm tall. The smaller, inner tube is used to supply the gaseous fuel to the burner mouth. The outside tube is used to supply the oxidizer. In the bottom of the burner, there is an encapsulated set of glass spheres 3 mm in diameter. These are present to reduce the turbulence of the incoming oxidizer stream. At the top of the burner,

there is a honeycomb mesh of 1.5 mm cell size. This mesh is present to ensure the oxidizer stream is non-turbulent when it reaches the burner mouth. All flames produced were checked visually to verify that they were laminar. This was done by making sure the flames had constant flow characteristics and that no vortices were present. An image of a methane/air flame and methane/oxygen flame can be seen in Figure 17.

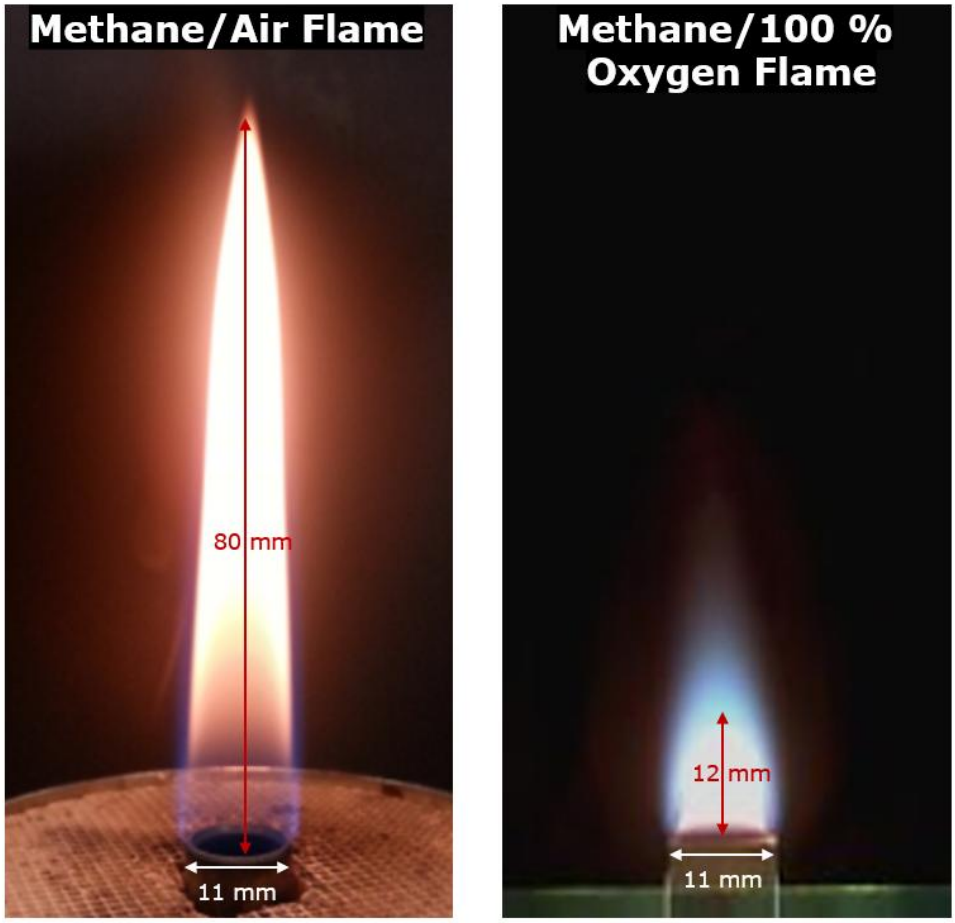

Figure 17: Methane Flames at Various Oxygen Concentrations

In the figure, no vortices are present in the flames at the selected test conditions. The flames appear to be of constant structure and are approximately symmetrical along the vertical axis. This was done to verify that the flames studied are qualitatively laminar.

The Reynolds number (Re) for the mouth of the burner was also calculated to verify the flame is laminar. This is done as Reynolds number is the ratio of inertial and viscous forces in a fluid, and is used to determine the fluid flow patterns. It was calculated using Equation 6.

$$Re = \frac{u \cdot L}{\nu} \tag{6}$$

Where u is the flow velocity, L is the characteristic length (in this case internal diameter), and v is the kinematic viscosity of the fluid in question. This value was found to be approximately 56, which is far lower than the threshold of 2300 which defines turbulence.

It can also be seen that the methane/oxygen flame is much shorter. This is due to the faster burning in the oxygen enriched environment. This fact determines the usable flame volume for sampling, and effects the HAB's (heights above burner) that can be sampled for this flame condition. This is showcased later in Chapter 6. It can be seen in the figure that the oxygen flame appears to extend beyond what is designated as its flame height. This is because flame height is typically defined in the literature as "luminous" flame height, which is flame the highest part of the flame structure that can be resolved visually. More flame structure is apparent in this image as a higher contrast was used in imaging, due to the higher luminosity of these flames.

It should also be noted that the apparent color of the two tested flames is different. The methane/air flame showcases yellow/orange throughout the flame volume. This is due to the larger soot population in the flame, resulting in more blackbody radiation and a yellow/orange glow. This is not seen in the methane/100% oxygen flame, indicating less soot is present, which will be verified in later sections.

Finally, the testing conditions for the flames must be discussed. Table 3 showcases the experimental conditions for each studied flame.

Table 3: Testing Conditions for the Studied Flames

Studied Flames	Oxidizer Flow Rate (cm^3/s)	Methane Flow Rate (cm^3/s)	Flame Height (mm)
Methane/Air	635	7.5	~80
Methane/100% Oxygen	635	7.5	~12

Listed in the table are the oxidizer flow rate, the fuel flow rate, and the apparent flame heights for each flame tested. These flow rates were controlled using Aalborg P-type rotameters and are verified by Aalborg digital flow meters. The flow rates for the oxidizer and fuel were kept constant for the two flames studied, as this maintains constant jet velocities and flow conditions.

3.2 Chemical Structure of Methane (CH_4)

In this work, the hydrocarbon methane (CH4) was chosen due to a variety of reasons. Firstly, methane was chosen due to its prevalence of use in the energy sector. Methane is the main constituent of natural gas, making up between 70% - 90% by volume of natural gas depending on the source [31]. This means that to understand the emission characteristics of natural gas, methane's emission characteristics must be studied as well to understand the bulk characteristics. Secondly, methane/natural gas is presented as a "clean" alternative to coal and other heavier hydrocarbons due to lower levels of sulfur and mercury contained within, meaning less emission of these harmful chemicals when burned. It is also a "cleaner" burning fuel due to its simpler chemical structure, meaning it produces fewer pyrolysis products. Finally, in recent years, methane has become a popular fuel for rockets. SpaceX's Raptor engine, Blue Origin's BE-4 engine, and a slew of others utilize methane as their fuel. Understanding the emissions behavior of this fuel is important to prevent coking (soot buildup) in engine components such as pre-burners, fuel injectors, and valves.

Methane's chemical structure consists of one carbon atom covalently bonded to four hydrogen atoms in a tetrahedral shape. With only one carbon for every four hydrogen atoms, there are plenty of chemical bonds to harvest energy from while only producing one free carbon atom that can then go on to become CO_2 or soot. Other fuels like ethane (C_2H_6) and propane (C_3H_8) have more bonds, but due to additional carbon atoms being present, they have a lower energy release per free carbon atom produced ratio. This metric is commonly defined as the H/C ratio (hydrogen to carbon ratio), and is used to provide insight into the energy content of fuels and their emissions behaviors. In this context, methane with a H/C ratio of 4, when compared to ethane's and propane's H/C ratios of 3 and 2.67, shows that methane will produce more energy with less emissions on a per carbon atom basis when compared to ethane and propane. This means that this fuel will release more energy per free carbon atom produced than the other two, leading to a "cleaner" burn.

3.3 Motion Control System

The thermophoretic sampler is hard-mounted to an optical table, and for sampling at various flame locations, the burner is moved using a motion control system. The motion control system consists of a 2-D UniSlide assembly (MA 6000, Velmex Inc.) that is driven by an 8300 series stepping motor. The co-flow burner is mounted to this UniSlide and is controlled using a laptop computer running the "Computer Optimized Stepper Motor Operating System (COSMOS V3.1.4)" software. This enables the moving of the burner in the X and Y directions with high precision (0.0000625 inches). For sampling and temperature measurement, the lit burner is positioned to where the location of interest is in line with the pneumatically driven piston. This allows for insertion of the sampling grind/thermocouple into the flame location of interest.

3.4 Thermophoretic Sampling

Thermophoretic sampling is used in this work to gain insight into how soot morphology changes with oxygen content, both primary particle diameter and nanostructure. This method was first pioneered by Megaridis and Dobbins [32]. It relies on the thermophoretic deposition of soot particles onto a carbon substrate covered grid. Thermophoretic deposition is when hot particles "freeze" onto a colder medium due to a temperature gradient. This allows for the sampling of delicate particles such as soot. This sampling is achieved using TEM grids that consist of a copper mesh grid covered with a thin carbon substrate. More information about the TEM grids can be found in a later section.

These TEMs are used to sample soot within flames by rapidly placing them in the flame for a short time. This is done with a pneumatic actuated cylinder. A visualization of this process can be seen in Figure 18.

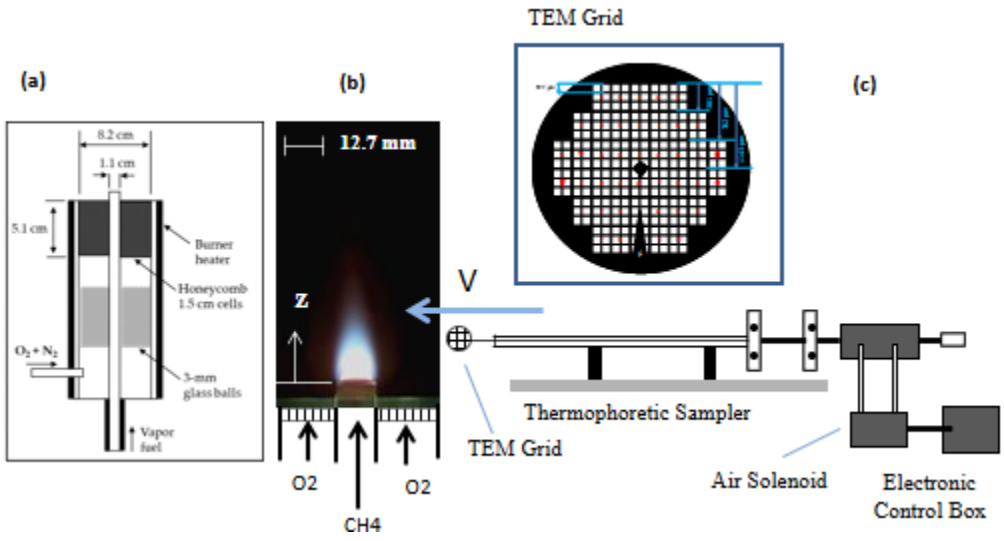

Figure 18: Schematic of Thermophoretic Sampling Using a TEM Grid [14]

As can be seen, a flame is generated by the co-flow burner. The TEM grid is inserted for a period known as the residence time and then removed. The total time the grid is in motion is known as the travel time. Residence time is an important consideration when using thermophoretic

sampling with TEM grids. The grid must remain in the flame long enough to collect sufficient soot for analysis, but not so long that the carbon substrate of the TEM grids could get too hot and potentially sustain damage. Fast travel times are also desired as this limits the grid's time in flame regions not of interest, reducing the amount of particulate contamination for these regions.

3.5 Transition Electron Microscopy

3.5.1 H2 Finder Grids

Due to the flame the reduced height of methane/100% oxygen flames it would be difficult to use a 3 mm diameter TEM grids to sample multiple heights within the flame. To be able to sample these flames at various heights, a special TEM grid known as the H2 finder was utilized. This grid includes microscopic letters and numbers to denote different spatial areas on the grid. Figure 19 shows the layout of the H2 finder grid.

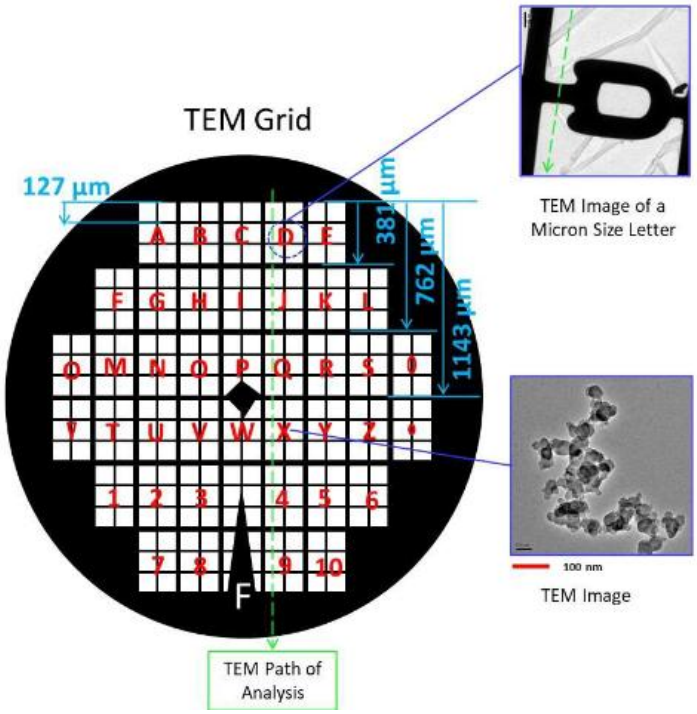

Figure 19: H2 Finder Grid [14]

This grid is copper and has a thin layer of carbon substrate laid over one side that acts as a capture reservoir for particulate matter. The grid is 3 mm in diameter. It contains a grid pattern that is of x columns and y rows. Each subsection is denoted by either a number or a letter, A-Z and 1-10, respectively. These symbols are only a micron tall and can be seen in the close-up for the image. These letters help divide the grid into smaller discrete areas, meaning that multiple soot samples at various heights may be sampled simultaneously, instead of only 1 sample height as with the regular grid. This allows for the sampling of flames with heights that are not suitable for regular grid use. The grid also includes an inverted "V" shape at the bottom. The point of this "V" is used to make sure the centerline of the TEM grid is in line with the central axis of the flame.

3.5.2 Electron Microscope

After the soot samples were collected, they were analyzed via a JEOL TEM-3010 microscope. The microscope was operated with a LaB6 filament and 200 KeV (kiloelectron volt). A series of images at low, medium, and high magnification was taken for all flame conditions. Low magnification images were used to compare overall soot density and degree of agglomeration for the test conditions. Medium magnification images were used to determine average primary particle diameters. Finally, high magnification images were used to conduct fringe-based analysis to determine changes in fringe length, tortuosity, and fringe spacing.

3.6 Flame Temperature Measurements

Flame temperature measurements were also conducted for each test case. This was done using a K-type thermocouple and temperature readout equipment. The thermocouple was attached to the probe that was inserted into the flame. For the flame measurements, a protocol was used. Once the thermocouple was placed within the flame, the temperature reading was allowed to rise until it leveled off. This is so that the thermocouple junction can come to equilibrium with the flame it is engulfed in. The thermocouple's voltage response is temperature dependent, so this was done

to ensure the flame readings being taken were accurate. Once the temperature readout had leveled off, temperature measurements were taken every 5 seconds until the temperature readout began to drop off. Figure 20 illustrates this thermocouple response behavior.

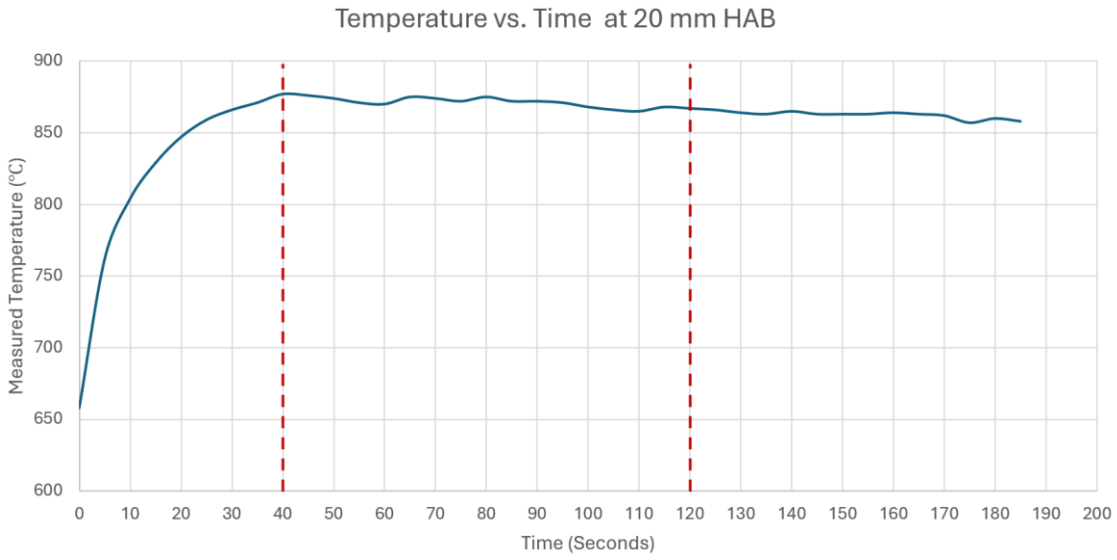

Figure 20: Measure Flame Temperature vs. Time to Illustrate R-Type Thermocouple Response with Red Dotted Lines Representing Boundaries of Data Used for Means

Figure 20 also shows how this data was trimmed to be able to calculate a representative average of the temperature at each HAB. The vertical red dotted lines are the upper and lower limits for the range of data used. For the lower boundary of this range, a temperature where the initial thermal soaking of the thermocouple was complete was chosen. Once the response curve had leveled off, this was defined as the start of the range, which is 40 seconds in this figure. The upper boundary of the range was chosen based on a gradual decline in temperature read by the thermocouple. This was determined to be the cutoff as the drop off is a sign of soot buildup on the thermocouple, effectively insulating it from the flame and skewing the readings. For example, this was chosen to be 120 seconds. After trimming, the values gathered for that spatial position in the flame are averaged, and the process is repeated for various locations to paint an image of the temperature field of the flame.

Chapter 4: Image Processing/Fringe Analysis

To obtain insight into the nanostructure of soot, it is not only required to take high-resolution TEM images, but also to process and analyze these images to be able to get useful quantification from them. To do this, the images but be altered to highlight the interior structure of the sampled soot. To achieve this, a MATLAB script was developed in-house based on the work of Yehliu et al. [33]. Their algorithm is widely used as a baseline in other similar studies [34,35]. This algorithm was chosen due to its ability to provide clean, easily discernible fringes, but also its ability to get the metrics of fringe length, tortuosity, and spacing from an image. Various image processing techniques were employed to pre-process these images. Table 4 lists the operations used and their associated values. These values were used based on recommendations of [33].

Table 4. Image Processing Parameters

Image Processing Operation	Shape/Size/If Used
Negative Transformation	Yes
Gaussian Low-Pass Filter	Standard Deviation = 1.0 Kernel Size = 11
Top Hat Transformation	Structuring Element Size = 5
Morphological Opening/Closing	Structuring Element Size = 2 Structuring Element Shape = Disk
Binarization	Ostu's Method
Branch Pruning	Spur Size = 2

While every step of the algorithm is discussed in the Yehliu et al. paper, a basic understanding would be beneficial to the reader. The basics of this image processing algorithm start with taking in a TEM-produced grayscale image in the form of a .tiff file. Next, a negative transformation must be performed on the image. This effectively flips the intensity of the image. This makes the dark regions light and the light regions dark and allows for simpler processing steps. Then the

algorithm needs the ability to let the user select a region of interest (ROI). Only the area of the image that contains the soot particle is of interest. The next step is to binarize the image. This is where a greyscale image is converted to black and white. To do this, there must be an intensity threshold set so that everything above the threshold is turned white and everything below is turned black. This threshold's value had a major impact on nanostructure parameters and was found by Pfau et al. [36], and following their recommendations, a method called the Ostu method was utilized to find the optimal threshold for the binarization. This method works by creating a histogram of the image's intensity values and using that to determine a threshold that maximizes the between-class variance. According to Pfau and colleagues, the Otsu method yields the best visual results for fringe analysis and provides the most fringes when compared to other thresholds. Because of this, the Otsu method was utilized for this work. Next, the binary image must be skeletonized. This process reduces the foreground regions of the image to 1-pixel-thick branches, known as fringes. This thinning of the foreground regions provides a simplified version of the feature, making quantification easier. Another step that must be taken is to set limits on what data to include. Fringes found to be less than 0.246 nm in length were considered artifacts of the pre-processing step and were excluded. This length was chosen as it is the diameter of one aromatic ring [37].

4.1 Preprocessing Steps

Negative Transformation

Before any useful metrics can be taken from the nanostructure of a soot particle. The HRTEM images must be preprocessed so that structures of interest can be easily identifiable for the image analysis. The first step in this process for fringe analysis of soot particles is to perform a negative transformation on the image. These images are usually in the form of a 8-bit, grayscale .tiff file. This negative transformation is needed to help highlight the graphitic layers within the soot particle. A comparison of an un-edited HRTEM image of a soot particle derived in a methane/oxygen flame and the same image with a negative transformation performed can be seen in Figure 21.

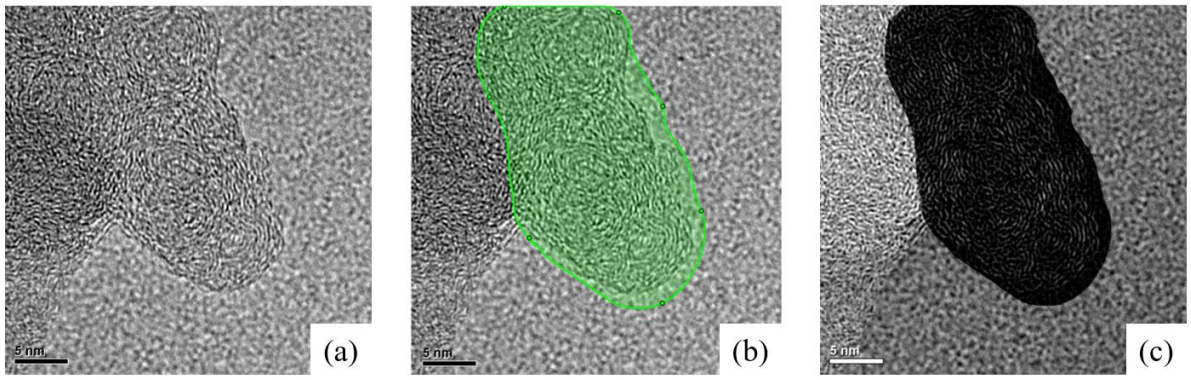

Figure 21: (a) Original .tiff Image; (b) User ROI Selection; (c) ROI with Negative Transform Performed

As seen in the figure, the graphitic layers of the soot particle show up as dark ridges in the unedited HRTEM image. This is due to the scattering or absorption of electrons emitted by the microscope, leading to darker regions where material is present. To enhance the appearance of the nanostructure, a negative transformation is performed. The negative transformation flips the intensity of the pixels of this image according to Equation 6

$$I_{negative} = L - 1 - I_{original} \quad (6)$$

Equation 6 is performed systematically on each pixel in the ROI of the image. Where $I_{negative}$ is the intensity of the pixel after the transformation, L is the number of intensity levels for the image (255 for 8-bit), and $I_{original}$ is the intensity of the pixels before transformation. In Figure 20 (c) after the transformation, lighter regions represent structure, and darker regions are background or the substrate of the TEM grid used for sample collection.

Region of Interest Selection

The next step in the image preparation process is to select a region of interest (ROI) for analysis. The MATLAB script developed lets the user draw a polygon around particles or aggregates to be analyzed. It then removes the data outside of the region of interest by forcing the pixels outside of it to an intensity value of 0. This ability lets the user manually choose what structures to analyze. Care must be taken to avoid areas that are difficult to analyze, such as multiple particle interference, and areas such as background substrate that do not have useful information to provide. Care also must be taken not to select small regions of the soot particle so that the fringe metrics measured are representative of the actual distribution of the internal structure. The soot has a core-shell structure that will be discussed in further sections. An example of this can be seen in Figure 21 (b).

Gaussian Low Pass Filter

A Gaussian low-pass filter is employed to help filter the TEM images. This is done to reduce background noise. It is also used to enhance the cohesiveness of structures by smoothing local intensity gradients. Both facts in tandem help to reduce potential spurious artifacts on a pixel level. The two parameters for this filtering are the standard deviation and kernel size. The values for these inputs can be seen in Table 4. These values were chosen based on the work of [33] and because they act to balance over-smoothing of features (can potentially merge features) and undersmoothing of features (leave high frequency noise behind). Though this technique can artificially change fringe metrics such a length, the same processing parameters were used for all images, meaning any skewing will be consistent, and trends should survive.

Top Hat Transformation

Top hat transformation is a morphological image processing operation commonly used in pre-processing scripts for fringe analysis. Its purpose is to enhance fine, bright features (soot fringes) by subtracting background morphology. This operation targets the spatial scale of features, whereas the Gaussian low-pass filter targets frequency components. Due to the spatial aspect of

the top hat transformation, the size of the structuring element must be larger than the noise features, but smaller than the fringes that are being resolved, so as not to erode them. Because of this, a structuring element of size 5 was chosen, with the shape being a disk to better smooth long curves.

Morphological Opening and Closing

Morphological opening and closing are a set of morphological operations that are used in fringe analysis to aid in the pruning process of fringes. Due to the turbostratic nature of soot, misaligned fringes can often be merged into to a single feature, typically resulting in structures that look like tree branches. This branching must be avoided as fringe length and tortuosity measurement functions do not properly measure these metrics. Because of this, branching must be minimized. At first, opening occurs, which is erosion, followed by dilation. This works to remove small bright objects and background noise. The next closing takes place, which the inverse of opening: dilation followed by opening. This process fills small holes and gaps that were made in fine structures (i.e., fringes) by the initial opening procedure. Even though these processes are effectively inverse operations, they affect the images in a nonlinear way, meaning that they do not precisely undo each other. This means they have a net effect on the image. Both processes are done with a kernel known as a structuring element. This structuring element is a small matrix that is passed over each pixel index of the .tiff image, applying the desired erosion or dilation operation. The structuring elements' shape and size are defined by the user. For this work, a disk structuring element of size 2 was chosen. A disk structuring element has a radius of 2 pixels. This process was applied using built-in MATLAB functions in the Image Processing Toolbox.

Binarization (Otsu’s Method)

The image must now be binarized. Binarization is the process of turning every pixel to either the maximum or minimum intensity value, black (255) and white (0), respectively. This is done by scanning through the image and reading the intensity value of the current pixel. If this intensity is

above a determined threshold, the pixel is set to black, and if below the threshold, it is turned to white. The determination of this threshold is the topic of many works, but there is agreement in the literature that one specific method should be used to maximize feature count. This method is known as Otsu's method, named after Nobuyuki Otsu, who first proposed the method in [38]. This method automatically determines a numerical value for binarization thresholding. It does this by scanning the image and testing different thresholds to find the threshold that maximizes inter-class variance. Inter-class variance is the difference in relative intensities for the foreground and background of the image. It is best to maximize this value as it minimizes the image data loss from converting from a grayscale image to a black and white image. Due to these reasons, Otsu's method was performed to determine the binarization threshold for the images, with the numerical threshold being recorded for each processed image.

Clearing Fringes from ROI Border/ Setting Minimum Fringe Length

Two intermediate steps to the image processing method are clearing fringes around the ROI border and removing short fringes from the measurement. The former is necessary due to the way the ROI is selected. Since the ROI is selected manually by the user, and typically soot primary particles (the interest of measurement in this work) are part of larger aggregates, the ROI selection will segment fringes as it is drawn. This can lead to shorter than actual fringes being recorded, thus skewing results. Because of this, fringes that intersect the ROI border are removed. This is done using a built-in function in MATLAB, which uses connected component labeling to remove fringes that touch the ROI border.

The second intermediate step that requires discussion is that of setting a minimum fringe length. Since fringes represent stacked graphene planes that are composed of aromatic rings, any feature resolved that is less than the diameter of a single aromatic ring (0.246 nm) is excluded. This length was suggested by [37]. This is because anything below this length cannot represent an actual fringe and, therefore, is most certainly an artifact of image processing. This is done after the feature identification step, and fringes below this length are marked so that they are not counted in subsequent steps.

Skeletonization

Once binarization is complete, the features present in the image must be skeletonized. This is a term for reducing a feature or a path down to a 1-pixel-thick line. This is done to enable quantifying fringe metrics such as length, tortuosity, and fringe lattice separation by making the structures digestible, while still preserving the general structure of the features. This was done using a built-in MATLAB function. Figure 22 shows the final skeleton of a soot particle along with the original TEM image for comparison.

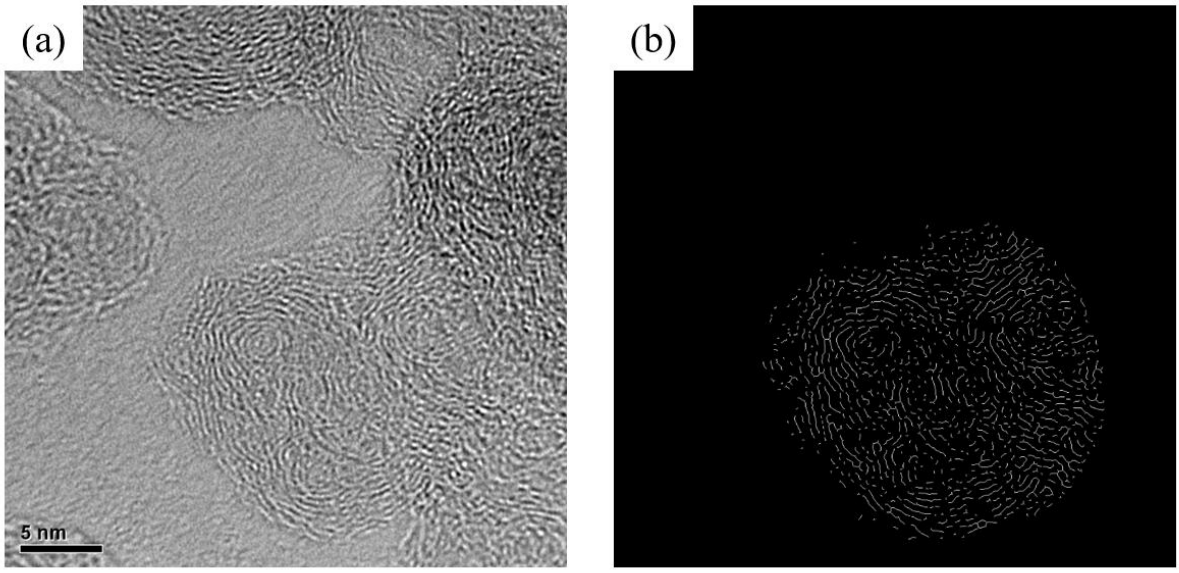

Figure 22: (a-b): Images of (a): Original Soot TEM Image and (b): Final Skeleton of Soot Particle

4.2 Fringe Characterization

Fringe Lengths (Path Lengths)

Fringe length is defined as a measure of the physical extent of the atomic carbon layer planes. It is an important metric as these lengths are positively correlated with a high degree of in-plane similarity with graphite. This provides the ability to assess the order of the crystal structure within soot particles. Since the fringes are reduced to 1 pixel thick during skeletonization, they have been inherently discretized into discrete pockets, i.e., pixels. This means that to approximate the length of the true curve in a continuous domain, the pixels must be counted. The distance between the centers of two adjacent pixels is 1, with this distance being √2 for diagonal pixels. To measure fringe length, the center of pixel to center of pixel distance is measured by summing all the center-to-center distances in each fringe. Then a correction factor of 1 is added to the final sum to account for the two half pixels that are not counted at the end points due to the center-to-center counting. This method of correction is only semi-valid, but much of the literature does not account for this error at all, and at a maximum, it only makes up a small percentage of the minimum fringe length.

Euclidean Distance Between Endpoints

Another distance metric of interest for soot nanostructure quantification is endpoint Euclidean distance. This is the straight-line distance between the two endpoints of the fringe. This distance is important because it allows for the calculation of another important metric, known as tortuosity. Tortuosity is the ratio of the path distance of a fringe to the Euclidean endpoint distance. More details about tortuosity can be found in the next section.

Euclidean endpoint distance is measured by using the Euclidean distance formula, as seen in Equation 7.

$$d = \sqrt{(x_2 - x_1)^2 + (y_2 - y_1)^2} \quad (7)$$

Where d is the distance between endpoints, x_1 and y_1 are the Cartesian coordinates for one endpoint, and x_2 and y_2 are the Cartesian coordinates for the second endpoint. These coordinates are defined by the pixel Cartesian coordinates for each endpoint.

Tortuosity

Tortuosity is a metric that is used to measure a path's deviation from a straight line. For fringe analysis in soot research, it tells researchers the curvature of fringes. This can be used as a measure of structural disorder, as the more curved fringes decrease graphitic spacing, making the material deviate from the ideal crystal structure of graphene. It has multiple definitions, but for this work, tortuosity is defined as the ratio of the length of a fringe to the shortest straight-line distance between the path's endpoints. This relationship is expressed in Equation 8

$$Tortusity = \frac{Fringe\ Length}{Euclidian\ Endpoint\ Distance} \quad (8)$$

Fringe Spacing

Fringe spacing is the distance between adjacent layers in a fringe lattice. This metric can inform researchers on maturity, oxidation rates, and the degree of graphitization. An illustration of the measurement of fringe spacing can be seen in Figure 23.

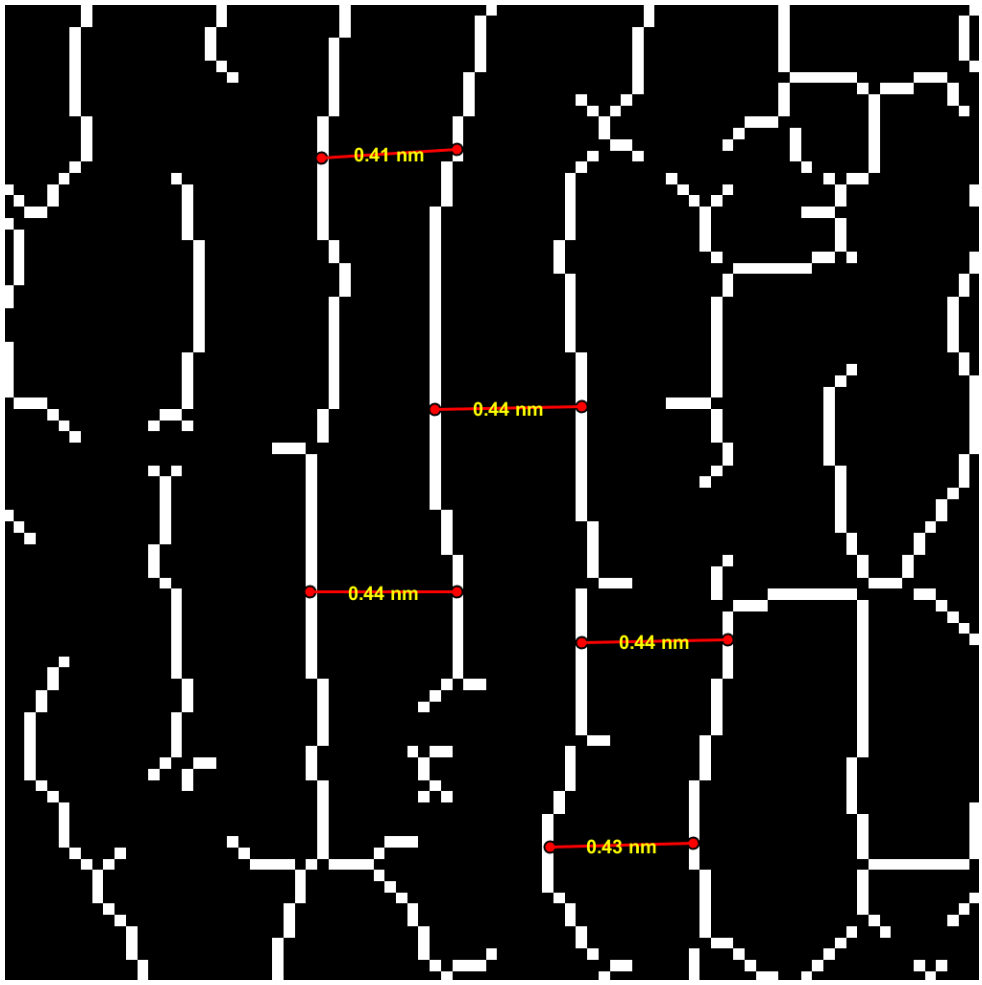

Figure 23: Illustration of User Fringe Lattice Spacing Measurements

Various works have measured fringe lattice spacings [34,35,36]. Some of these researchers calculate the average distance between two adjacent fringes. This is a difficult process since soot fringes are present as curved structures, but are not always parallel to their neighbors. This measures the perpendicular distance between fringes. This process is also difficult to automate as computer algorithms commonly match image features as fringe pairs, even though the features identified by the algorithm for this might be image processing artifacts. Yehliu et al. [33] attempted to tackle these issues by having their image processing program let the user choose fringe pairs. Their program then trims the two fringes to similar lengths, using the initially shorter fringe as a reference point. The program then measures the perpendicular distance from one fringe to the adjacent fringe along the length of the pair. It was decided not to use this approach for this work due to implementation complexity. Instead, the algorithm developed here

allows the user to manually place points to measure in between adjacent fringes. Each successive pair of user-placed points is one distance measurement. The distance between the two points is calculated using the Euclidean distance formula, as previously discussed. The user is allowed to place as many point pairs as they please, and then they prompt the program to end the graphical measurement stage. Once the program has been prompted to do so, it tabularizes the measured distances for further analysis later.

Code Verification

Verification of code written for metric measuring is essential to making sure any quantitative measures taken are valid. This was done in a variety of ways. For the fringe length and tortuosity script, a verification image was created to validate the code's measurement outputs. Various arcs of different shapes and orientations were chosen to verify that the script's measurement and exclusion were valid. This verification image can be seen in Figure 24.

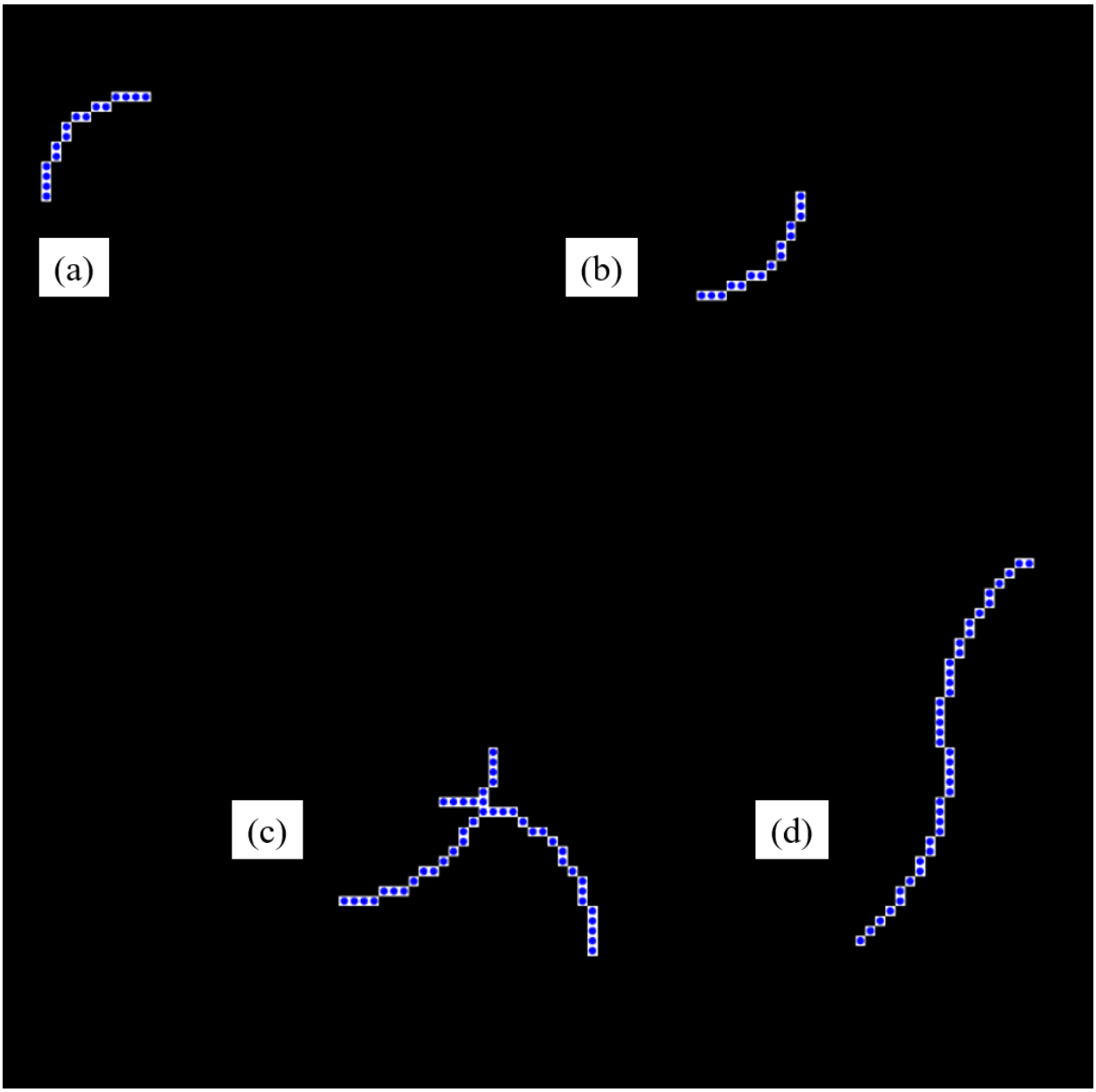

Figure 24 (a-d): Script Verification Image with Multiple Features (a-d)

In the figure, 4 features can be seen on a black background. This was to simulate the curved fringes seen in soot nanostructure. The blue dots present within the features indicate the center of each pixel. This was to allow for manual counting/measuring of feature length to verify the code against. Features a and b are arcs of the same dimensions, just rotated 180 degrees off one another. They were chosen to show the script that could recognize and correctly measure fringe length and Euclidean endpoint distance regardless of orientation. Feature (c) consists of two arcs

that create a junction. This is to verify that the code will recognize branched structures that did not get fully resolved by the various preprocessing steps, and exclude them from measurements. This is done because paths with more than two endpoints are not measured correctly by that path-making algorithm. Lastly, feature (d) shows a “switchback” arc. This feature was chosen to show the algorithm properly construct paths that might change direction. This is important to verify that the algorithm is properly calculating tortuosity.

This image is used as input into the fringe and tortuosity measurement script. Figure 25 shows the output of this script, and Table 5 shows the metrics measured for each feature.

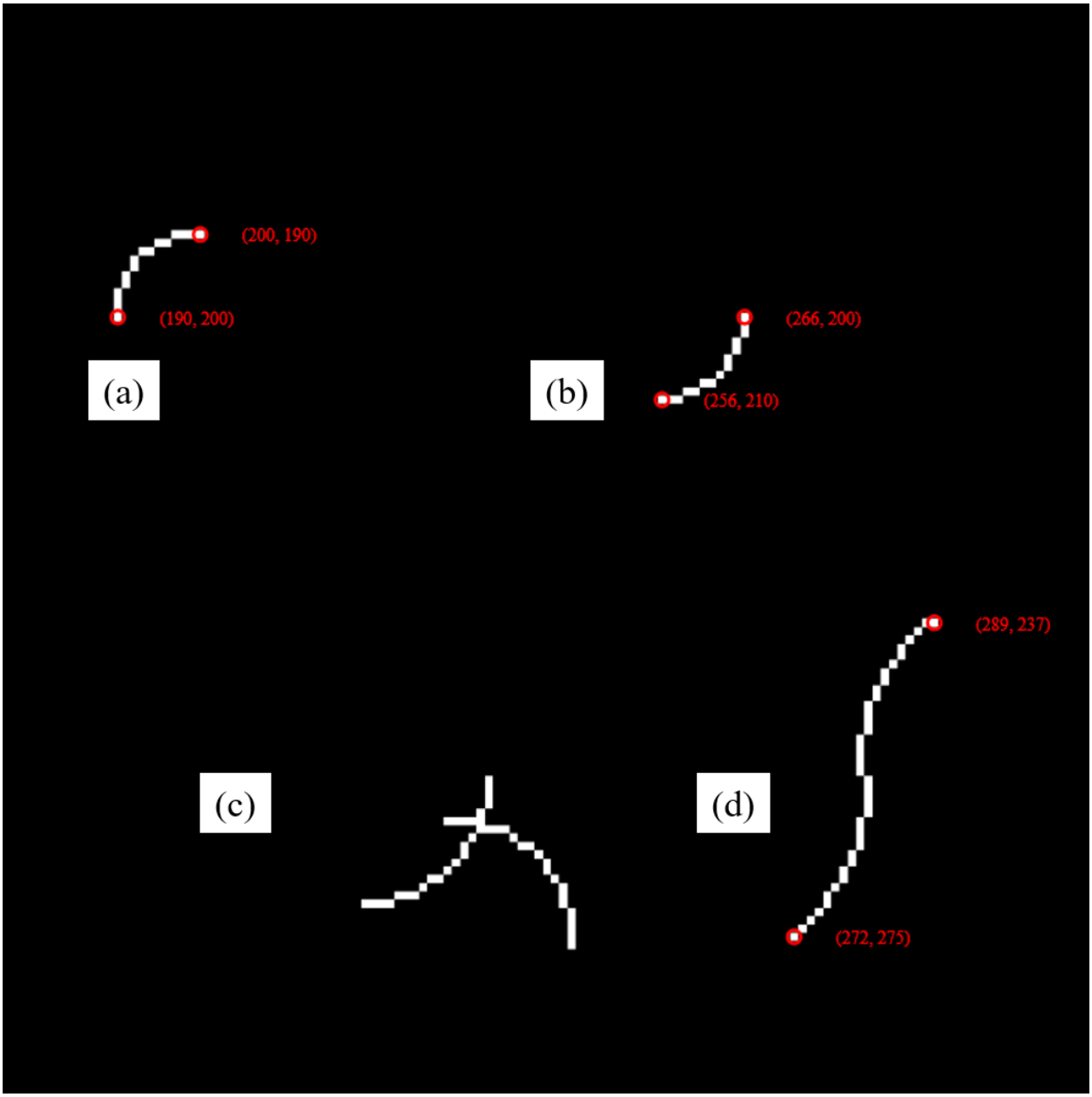

Figure 25 (a-b): Verification Image After Being Used as Input for the Fringe Length and Tortuosity Script with Features Labeled (a-d)

It can be seen in Figure 25 that this script properly selects endpoints for features (a),(b), and (d), as indicated by the red circles and associated x and y coordinates. Feature (c) does not have its endpoints visualized. This is because the code counts endpoints of features, and if the number of features exceeds 2, the feature is excluded from measurement. This lack of endpoint labels in

Figure 25 and the lack of measurement data from the scripts output window for feature c indicate that the code is properly filtering out branched features.

Path lengths were verified by manually counting pixels center to center, with straight sections being 1 pixel and diagonal center to centers being √2. 1 pixel was also added to the total length to account for the two half pixels excluded on the ends of a path. The code counts paths in the same fashion, so counting manually and then comparing the found numbers against the algorithm's output verifies if it is working as intended.

Euclidean endpoint distance is verified slightly differently. The code outputs Cartesian coordinates for each endpoint of a pixel, and it then uses Equation 4 to calculate the distance between the two endpoints in pixels. These endpoints can have their coordinates verified manually. The Euclidean distance between them can also be calculated to verify the code's output.

Finally, since path length and Euclidean endpoint distance have been verified, tortuosity is as well. Tortuosity is the ratio of these two other metrics, so its calculation is simple. Script output is verified against hand calculations for this metric.

Table 5. Verification Image Feature Metrics

Feature	Path Length (Pixels)	Euclidean Endpoint Distance (Pixels)	Tortuosity
a	18.071	14.142	1.278
b	18.071	14.142	1.278
d	47.456	41.629	1.782

Table 5 lists the fringe path length, the Euclidean endpoint distance, and the tortuosity for each of the verification image features. Features (a) and (b) are in good agreement, which showcases that the script will properly measure fringe metrics regardless of orientation. The metrics of all three features measured by the script match the hand calculations that were performed. This verifies that the script accurately measures these metrics.

The repeatability of all the developed scripts and the subsequent plots generated was ensured through the structure of the scripts. Each script was written so that any variable used is defined and has the user determine the numerical value at the beginning of the code. These values do not change unless the user specifies a different value. For the preprocessing script, the same filters/operations are performed in the same order, with no random or symbolic operations being done. This ensures that the same input image with the same ROI produces the same output image. This resultant processed ROI is then used as input for the metric scripts. Both metrics scripts were validated as described above and consistently gave the same outputs when fed the verification images. The only sources of variability in metrics measured are the initial ROI selection and manual measurement of fringe spacing. The former is a potential source of variation because if the ROI includes large amounts of TEM background substrate instead of just soot particles, it could skew metric measurement. The latter is a source of variation because the user manually measuring fringe lattice spacing might not always select a truly perpendicular path between the two fringes, leading to skewing of metrics. Both sources of variation are combated with documentation for future users detailing the importance of the drawing of the ROI and careful measurement of manual fringe lattice spacing. These sources are also combated by utilizing larger sample sizes, which help to dilute random errors.

Chapter 5: Analysis of Soot Particles Derived from Methane/Air Flames

This chapter's purpose is to present the evolution of soot produced in two laminar co-flow flames, one of methane/air and the other of methane/100% O_2. The particle density and spatial evolution of soot produced in these flames are characterized using low and medium-resolution TEM images taken along the centerline of the flames in the axial direction, at various HABs. The nanostructure evolution, i.e., potential changes in fringe length, tortuosity, and fringe spacing, is analyzed similarly. High-resolution TEM images were taken of soot samples at various HABs, and then in-house developed MATLAB scripts were used to quantify changes in nanostructure. The nanostructure of both flames is then compared to assess the effect of oxygen enrichment on

the soot produced. The results of these analyses are discussed in subsequent subsections of this chapter.

5.1 Soot Particle Evolution in Methane/Air Flames

Figure 26 shows low-resolution TEM images taken of soot sampled from the methane/air co-flow laminar diffusion flame that was sampled.

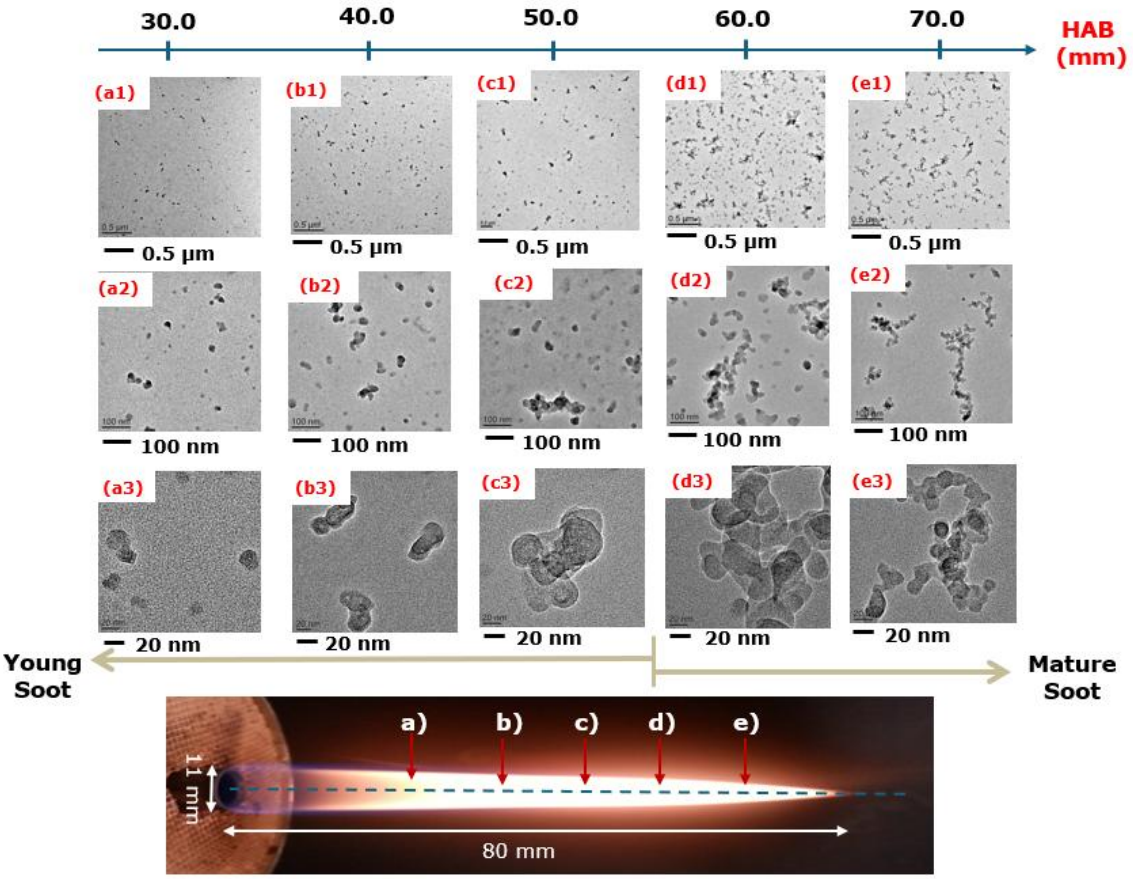

Figure 26: Soot Evolution Along Centerline Axis for the Methane/Air Flame

In Figure 26, low-resolution TEM images can be seen, with each image given a label for reference purposes. HAB is being used here to represent the height above the burner mouth in which soot samples are being taken and then imaged. These images were taken at HAB values of

30, 40, 50, 60, and 70 mm. Scale bars below each image indicate known distances for reference. Particles at lower heights (HAB <= 50 mm) are seen to be only single particles or aggregates composed of only a few primary particles. These are referred to as young soot due to the limited degree of agglomeration. Aggregates/particles sampled at heights above 50 mm are referred to as mature soot. This is because they showcase longer, more developed aggregate chains. The top two rows are being used to assess general particle density at each sampled height. With increased HAB, particle population density increases. This is expected as the height in the flame increases, more PAHs are present, leading to more soot growth. The middle row is used to assess how the degree of agglomeration of aggregates changes in the flame. Close to the burner mouth, only single particles and small aggregates composed of a few primary particles are seen. As HAB increases, however, aggregates are seen to be composed of more primary particles. This fact can be seen in more detail in the bottom row, which shows single aggregates imaged at medium magnification with TEM imaging.

Also seen in the figure, lower in the flame towards the burner mouth, young soot composed of single particles and small aggregates can be seen. As the soot goes higher in the flame, it starts to agglomerate into aggregates of 3-5 primary particles as it matures, and then towards the top of the flame, it peaks in aggregate size and then starts to decrease again at the very tip of the flame. This is likely due to higher oxidation rates at the tip of the flame. This growth of aggregates by agglomeration of more primary particles is expected.

High-resolution images were then used to qualify and quantify soot nanostructure in the methane/air flame. The images were taken at the same conditions as the low and medium resolution images, i.e., HAB. Figure 28 shows these high-resolution TEM images.

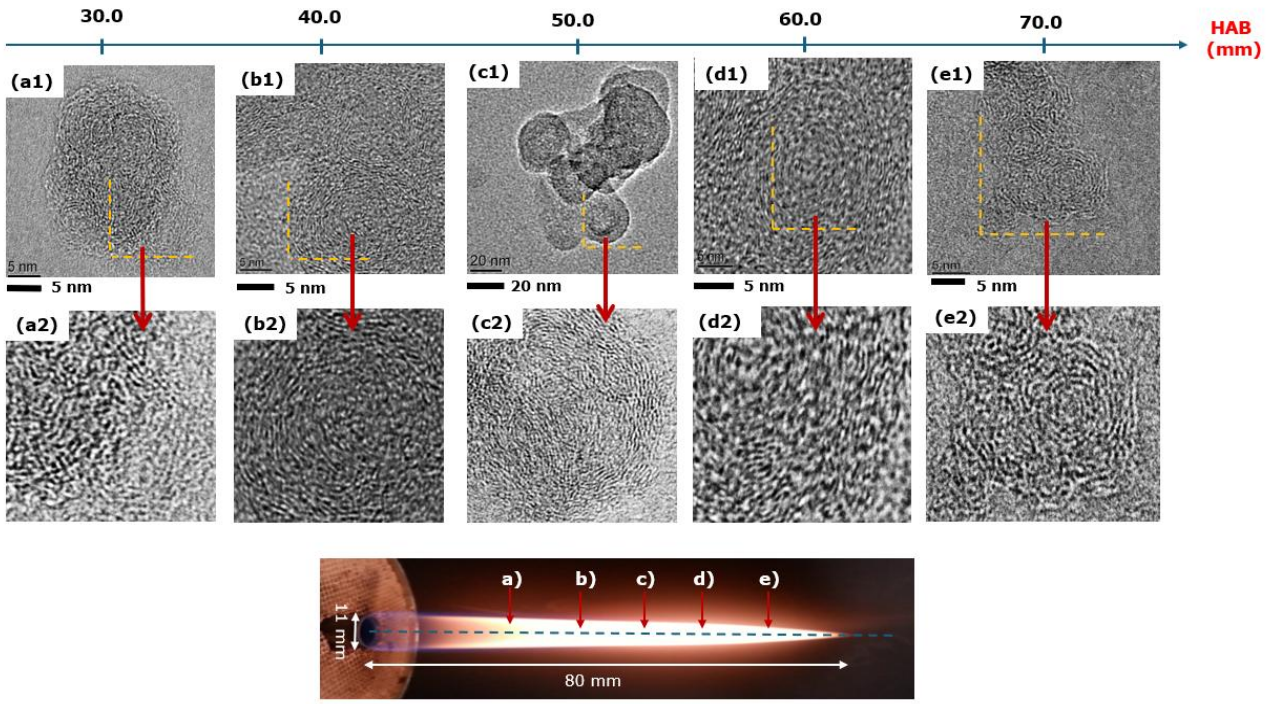

Figure 27 (a-e): High-Resolution TEM images showing the internal structure of soot morphology of particulates for samples collected at HAB = 30 mm (a1-a2); 40 mm (b1-b2); 50 mm (c1-c2); 60 mm (d1-d2); and 70 mm (e1-e2).

As shown in the figure, under high resolution, soot particles showcase a curved, layered carbon structure. In young soot (lower axial position), the internal structure appears to be composed of graphitic layers, with little structure, making it amorphous. Very early in the flame however, concentric rings are seen to form but then do not appear to increase their order of structure as the rise in the flame. In this more mature soot, stacked graphitic layers appear on the outside of the particles that compose the aggregates, while the center remains amorphous, as these cores were the amorphous soot precursors. This structure is known as a core-shell structure and has been observed previously by [39,40]. As the aggregates continue higher in the flame, they continue to grow in volume, adding more layers to their exterior. They then reach a maximum and then decrease in size due to increased oxidation at the flame tip.

5.2 Soot Nanostructure Metrics

Unedited HRTEM images can only provide qualitative information about the soot nanostructure. To be able to investigate if oxygen enrichment influences soot nanostructure, there needs to be a way to quantify the nanostructure to be able to make a meaningful comparison. This is facilitated using the method of fringe analysis, as outlined in detail in Chapter 3. This method involves the processing of the 8-bit grayscale .tiff images from the microscope to be able to quantify the soot fringes. After pre-processing, skeletonized ROIs are used as input for two scripts, one that automatically measures fringe length and fringe tortuosity, and one in which the user manually measures fringe lattice spacing. This is done across multiple primary particles, totaling 2000-3000 fringes sampled. The nanostructure metrics are then plotted as log-normal fits of histograms, with the y-axis being the frequency of certain values for the metrics and the x-axis being the measured value of that metric. The log-normal fits for each HAB are then compiled into a single figure to allow for a comparison of the trends. These log-normal plots for the methane/air flame are presented in the following figures, with Figure 29 presenting fringe length, Figure 30 presenting fringe tortuosity, and Figure 31 presenting fringe lattice separation. Tables 6-8 and Tables 9-11 are used to present the averages of each of these metrics at each HAB for the methane/air and methane/100% oxygen flames to analyze if these metrics change throughout the flame.

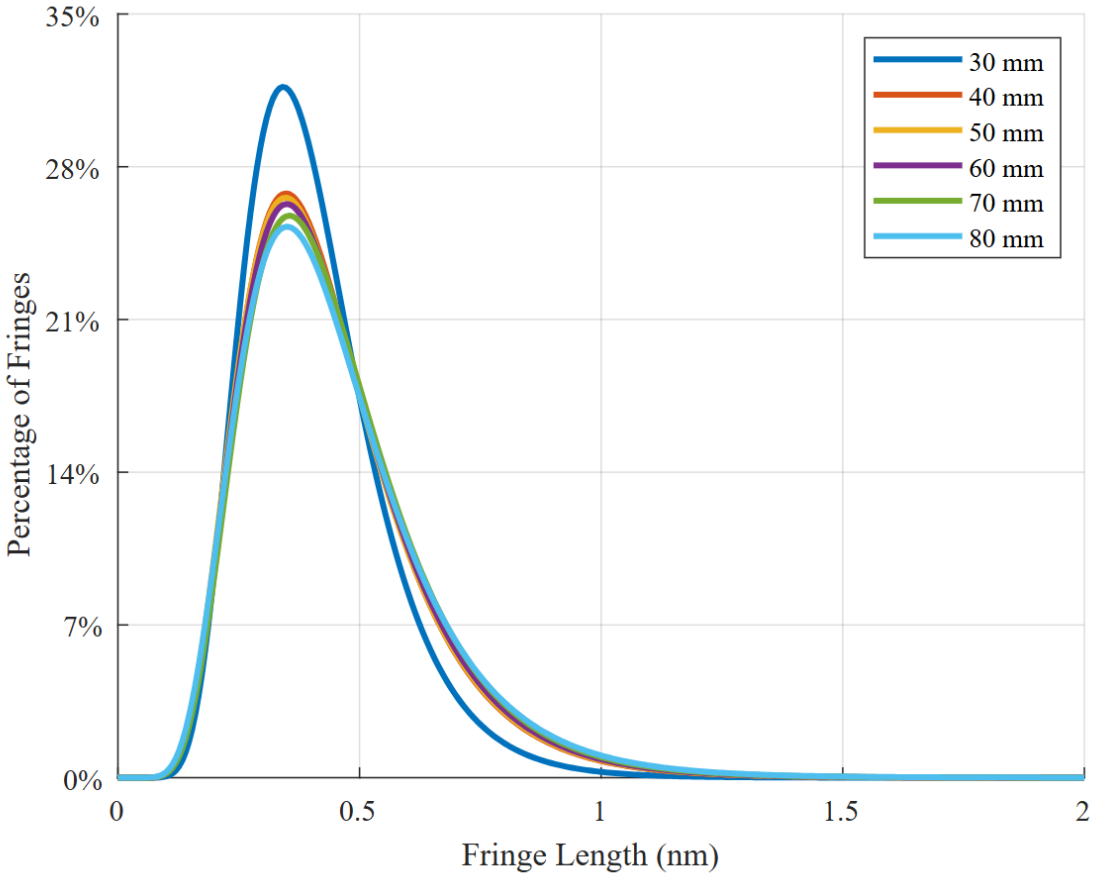

Figure 28: Log-Normal Fit Distribution of Soot Nanostructure Fringe Length at Various HABs for Methane/Air Flame

Figure 29 shows the log-normal fitted histograms for the methane/air flame at each HAB tested. All distributions are right-skewed and centered around 0.34-0.35 nm. This means that most fringes are short for all HABs, with consistent distribution across all HABs. The distributions are very close in shape. Most of the distributions peak in frequency between 25-27% of fringes, while the 30 mm HAB curve shows the highest peak of around 32% of fringes. This means that the peak frequency is highest at the lowest HAB, leading to the 30 mm HAB having the highest proportion of short fringes. The rest of the distributions match reasonably well, with slight decreases in peak percentage of fringes as HAB increases. A similar distribution agreement was observed by [41] in heptane flames. They found that there is little change in the distribution with respect to HAB, which is like the finding here. To dive deeper into the effect of HAB on fringe

lengths, various descriptive statistics for the distributions within the methane/air flame are listed in Table 6, including mean fringe length (FL), standard deviation (σ), and the coefficient of variance (σ/FL)

Table 6. Descriptive Statistics for Fringe Length Measurements in Methane/Air Flames

HAB (mm)	FL (nm)	σ (nm)	σ/FL
30	0.41	0.18	0.43
40	0.45	0.22	0.50
50	0.45	0.23	0.51
60	0.45	0.24	0.52
70	0.46	0.23	0.50
80	0.46	0.26	0.55

Various works have compared just the mean fringe length, but [???] claimed that only considering the mean can obscure structural changes in the soot, so other metrics like standard deviation and coefficient of variance are also considered to mitigate this. These distributional metrics are also considered when looking at tortuosity and fringe lattice spacing metrics later in this work.

As can be seen in the table, the average mean fringe length starts at 0.41 nm for the lowest HAB, increases to 0.45 nm at the next sampled HAB, and then does not change much until the tip of the flame. This showcases an initial spike in mean fringe length, and then very little change after that. This suggests a rapid initial structuring of the nanostructure, with little variation in fringe length with progression in the flame. This result matches that of [35,42], as methane is characterized as a non-graphitizing fuel. This means the carbon produced by the pyrolysis of methane is resistant to structural change. This is also shown in the coefficients of variance for the various HABs. There is initially a lower coefficient of variance, meaning the structure is more uniform in short lengths, meaning less structured soot. The coefficients of variance then increase at 40 mm HAB and stay relatively constant until the flame tip, meaning from 40 mm to 70 mm

HAB, there is little change in the wider distribution of lengths. Then, at the tip of the flame, the oxidation mechanism takes over and increases the variance even more. The standard deviation also increases throughout the flame, meaning that a larger proportion of the length is further from the mean.

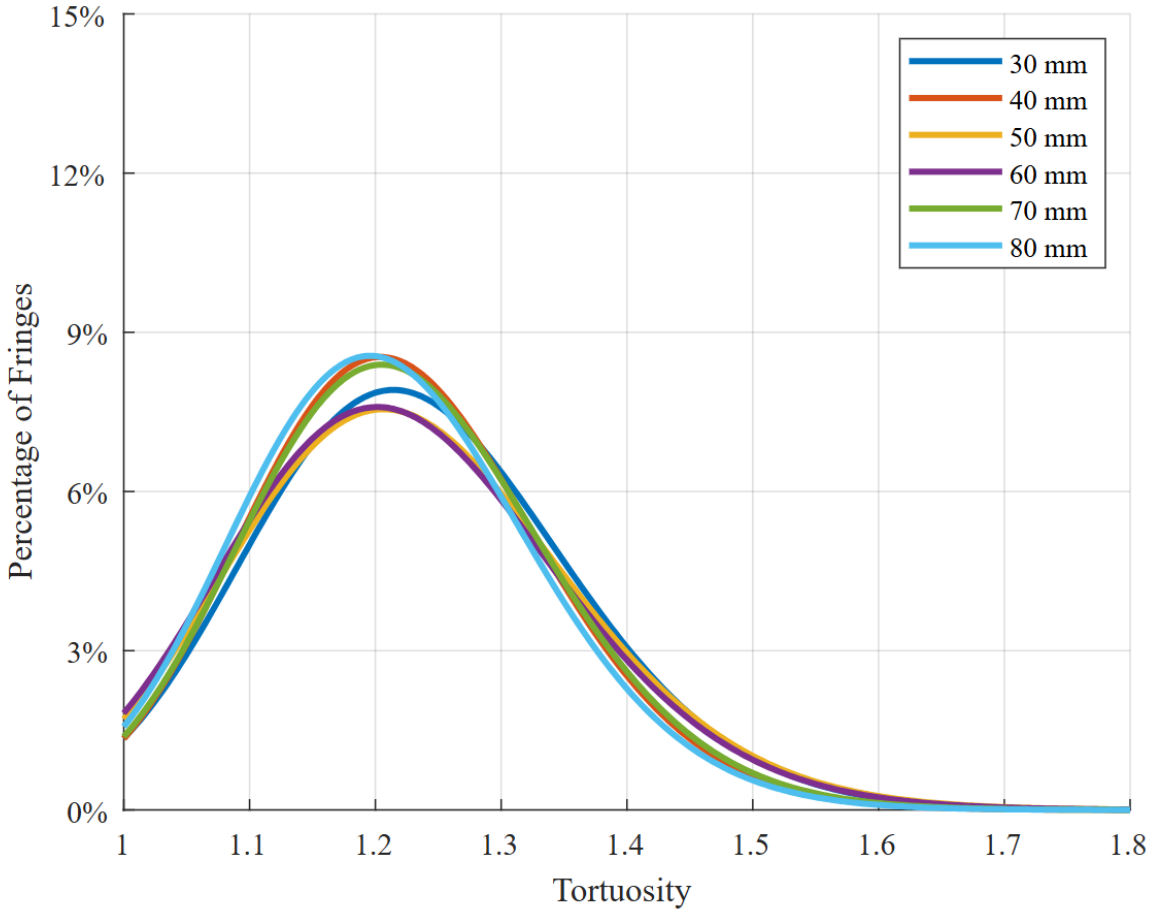

Figure 29: Log-Normal Fit Distribution of Soot Nanostructure Fringe Tortuosity at Various HABs for Methane/Air Flame

Figure 30 illustrates the log-fit distributions of tortuosity for the methane/air flame at various HABs. There is little variation in the respective tortuosities, with all of the fits showing similar shape and peak values. This suggests that tortuosity remains relatively unchanged with increased HAB. Further evidence for this can be seen in Table 7.

Table 7. Descriptive Statistics for Fringe Tortuosity Measurements in Methane/Air Flames

HAB (mm)	FT	σ	σ/FT	% FT > 1.5
30	1.235	0.15	0.120	4.9
40	1.222	0.14	0.133	3.9
50	1.229	0.17	0.140	4.5
60	1.225	0.21	0.174	3.8
70	1.223	0.15	0.122	3.9
80	1.214	0.15	0.126	2.9

In the table, mean tortuosity (FT), standard deviation, coefficient of variance, and percentage of fringes greater than 1.5 tortuosity are shown. This last metric was included for tortuosity to gain more insight into highly tortuous fringe evolution, as done in [34]. For mean fringe tortuosity, the tortuosity stays relatively constant with increased HAB. There is a slight decrease, however, suggesting slightly more ordered soot with increased HAB. This slight decrease is further supported by a decrease in the percentage of fringes with a tortuosity greater than 1.5. Oxidation preferably attacks more tortuous rings, so this is expected. These two points, along with relatively constant standard deviation and coefficient of variance, suggest a very slight effect on tortuosity throughout the flame.

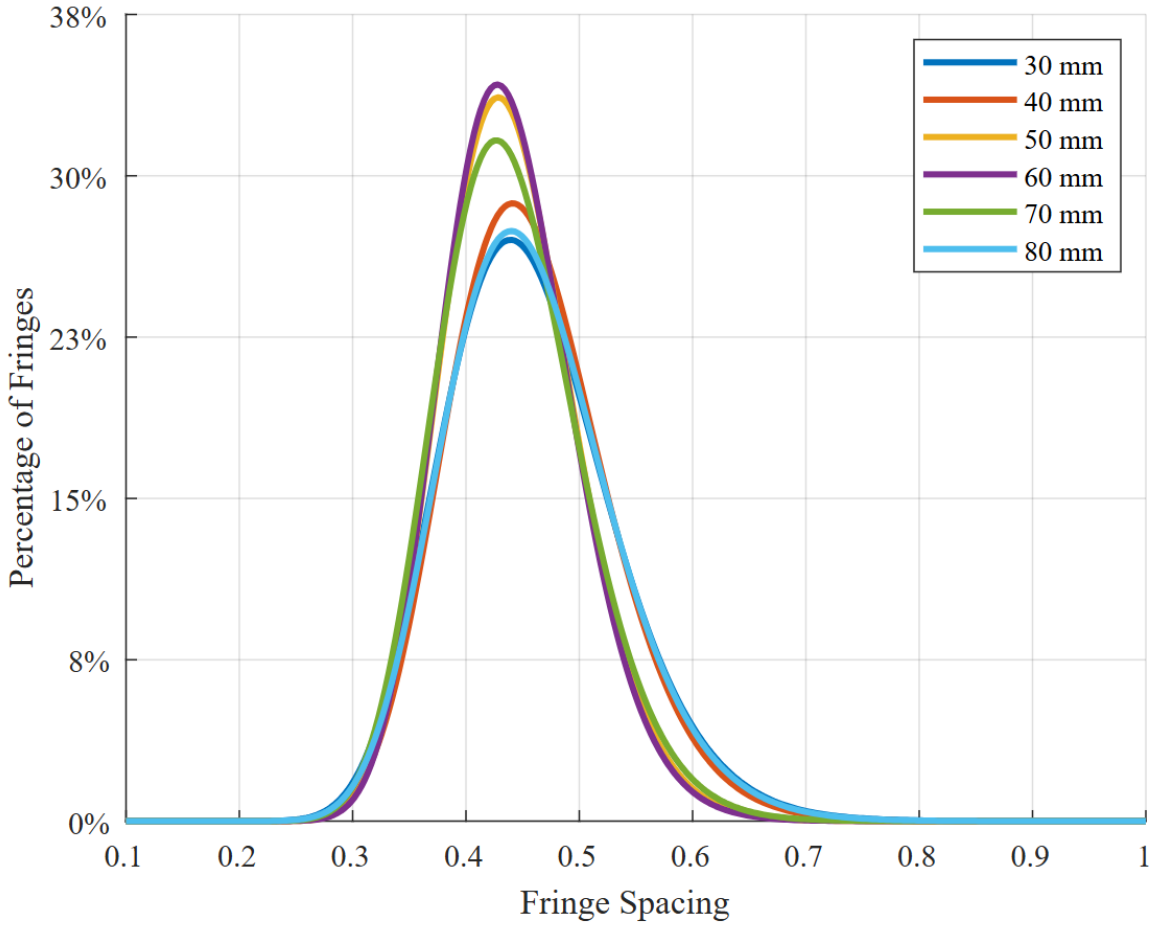

Figure 30: Log-Normal Fit Distribution of Soot Nanostructure Fringe Lattice Spacing at Various HABs for Methane/Air Flame

Figure 31 shows log-fit distributions for histograms of fringe lattice spacing at various HABs for the methane/air flame. All peaks showcase narrow, symmetric peaks, with peak values ranging from 0.42-0.44 nm, suggesting tight spreads in fringe lattice spacing for all HABs tested. There is no clear trend in fringe length with increasing HAB, with 50 mm and 60 mm HAB having the highest proportion of shorter fringe spacings. 30 mm and 80 mm HAB, the base and tip of the flame, respectively, have very similar trends. These two findings support the observation that fringe lattice spacing is not significantly affected by HAB. More evidence of this can be seen in Table 8.

Table 8. Descriptive Statistics for Fringe Lattice Spacing Measurements in Methane/Air Flames

HAB (mm)	FS (nm)	σ (nm)	σ/FS
30	0.457	0.073	0.16
40	0.457	0.068	0.15
50	0.440	0.057	0.13
60	0.439	0.057	0.13
70	0.440	0.062	0.14
80	0.458	0.076	0.17

Table 8 shows fringe lattice spacing metrics at various HABs for the methane/air flame tested. Mean fringe a lattice spacing (FS), standard deviation, and coefficient of variance are all considered. It can be seen in the second column that the mean fringe lattice spacing changes very little with respect to HAB. Low variation in standard deviation reinforces the assertion that fringe lattice spacing is narrowly distributed, further supporting the finding that soot nanostructure from methane flames is relatively unaffected throughout the flame volume.

5.3 Flame Temperature Measurements

The purpose of this section is to present temperature measurements that were taken from the methane/air flame that was studied in this work. All the temperatures are in Kelvin. The temperatures presented are averages of multiple measurements taken at each sampled flame location. It is important to note that the temperatures used to calculate the averages and those presented are from raw thermocouple readings or “uncorrected” measurements. This was done as different investigators use different correction techniques, and this work is only interested in trends, not specific measurements. Flame temperatures were not taken for the methane/100% oxygen flame due to thermocouple temperature and oxidation resistance issues.

For the methane/air flame, measurements were taken at HAB locations of 10 mm – 80 mm in 10 mm increments along the axial centerline of the flames. Radial temperature measurements were also taken at HAB locations of 40 mm and 60 mm. Both axial and radial flame temperature measurements are important to soot researchers as they help determine temperature fields within the flame and provide insight into the complex relationship between temperature and soot formation. Figure 32 shows the mean temperature distribution with respect to axial centerline HAB location for the methane/air flame used for this work.

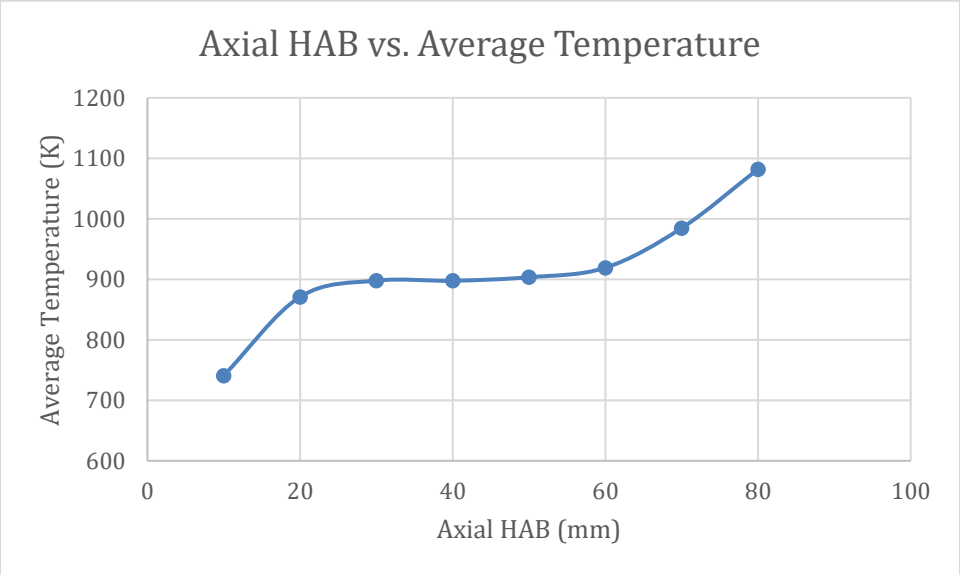

Figure 31: Methane/Air Average Temperature vs. Axial HAB Position

It can be seen in the figure that from HAB of 10mm – 30 mm, the temperature rises sharply and then begins to level out. From HAB 30 mm – 50 mm, the temperature levels out and stays roughly constant. Finally, from HAB 50 mm – 80 mm, the temperature begins to rise and continues to rise until the end of measurements. The shape of this trendline closely matches that of biodiesel/air flames studied by Merchan-Merchan et al. [23].

Chapter 6: Results/Discussion for Soot Sampled in Methane/100% Oxygen Flames

6.1 Evolution Profiles

Figure 33 shows low-resolution and medium TEM images taken of soot sampled from methane/100% Oxygen co-flow laminar diffusion flames.

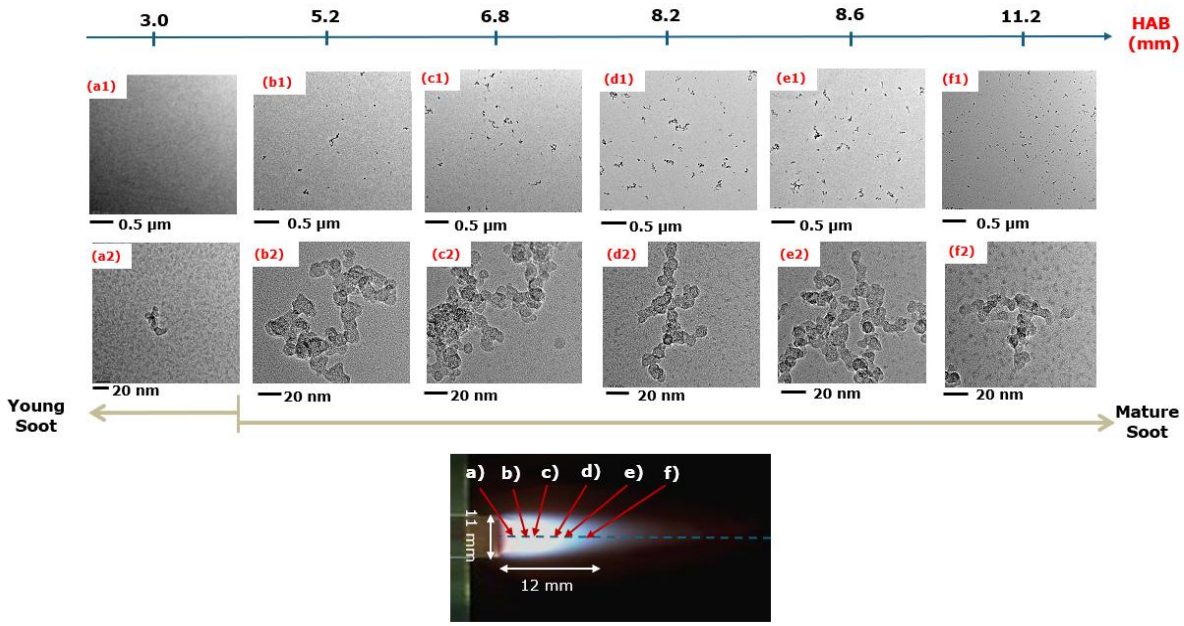

Figure 32: Low and Medium Resolution TEM Images of Soot Sampled from a Methane/100 % Oxygen Flame

As with the methane/air flame discussed in the previous chapter, various HABs were sampled, with the chosen flame heights investigated being 3.0, 5.2, 6.8, 8.2, 8.6, and 11.2 mm, respectively. These reduced HABs are due to the oxygen flames condensed flame volume. Scale bars and image labels are included in the figure as well. The top row are low resolution images while the bottom row is medium resolution images. Like the methane/air flame, the soot population density is low close to the burner mouth, grows in number as HAB is increased until it reaches a maximum, and then begins to decrease at the top of the flame.

Medium resolution TEM images were used to qualitatively study degrees of agglomeration. Like the methane/air flame, the soot for the methane/100 % O2 flame starts as single precursor particles, undergoes agglomeration into aggregates, reaches a peak aggregate size, and then decreases towards the top of the flame. Not only does the size of the aggregates themselves follow this trend, but so does the number of particles within the aggregates.

High-resolution TEM was also used to qualitatively study the nanostructure of methane/100 % O_2 flames. Figure 35 shows the evolution of soot nanostructure within the flame with respect to HAB.

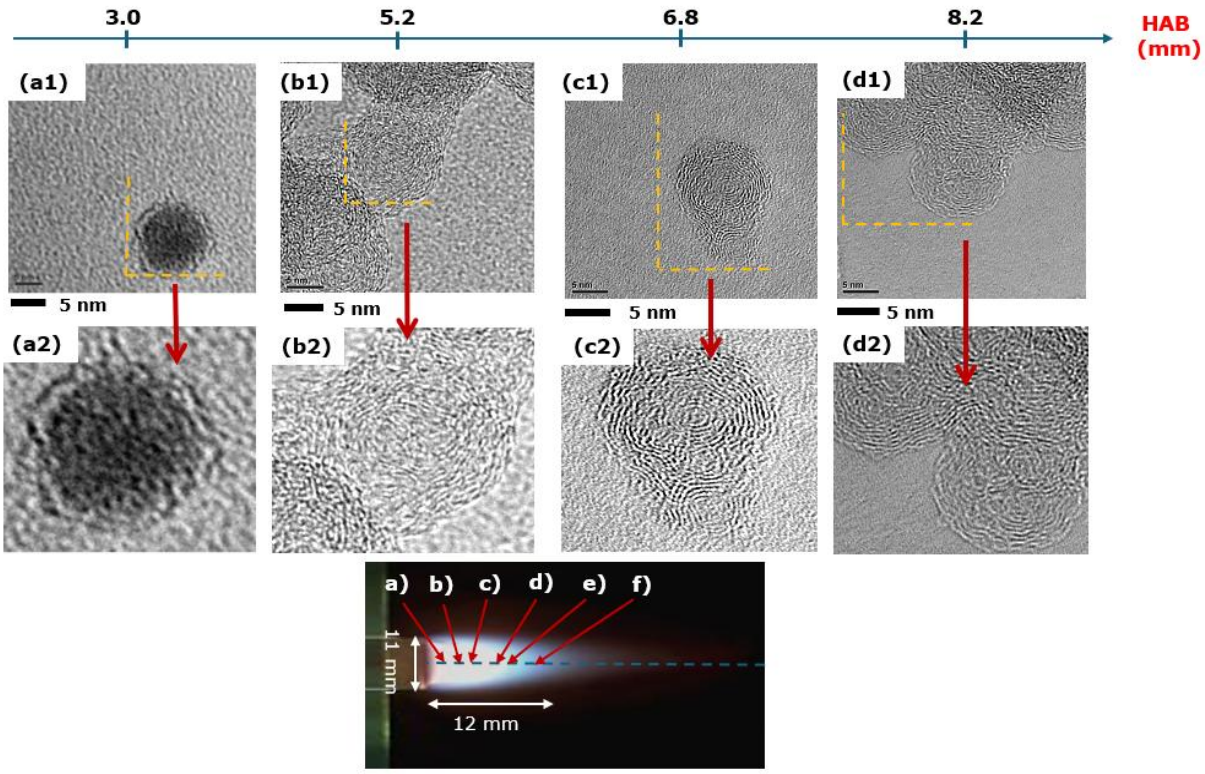

Figure 33 (a-e): High-Resolution TEM images showing the internal structure of soot morphology of particulates for samples collected at HAB = 3.0 mm (a1-a2); 5.2 mm (b1-b2); 6.8 mm (c1-c2); and 8.2 mm (d1-d2)

In the figure, HABs that were investigated were 3.0, 5.2, 6.8, and 8.2 mm. Like the methane/air flame, low in the flame, single particulates can be seen that consist of amorphous layers. This can be seen in (a1). Then at the next HAB, as imaged in (b1) and (b2), concentric graphitic rings

can be seen to form. Continuing up in the flame, the primary particles seem to grow in diameter and exhibit the core-shell structure previously described. However, similar to the methane/air flame, concentric rings are seen to form early in the flame, and then do not seem to change much in structure after that.

6.2 Soot Primary Particle Diameter

Another metric that is used to quantify how oxygen enhancement affects soot formation is soot primary particle diameter (d_p). This metric is used by other researchers to quantify the increased oxidation and formation rates of soot [21, 22, 23]. The work of [21] that was discussed in Chapter 2 has investigated this, but only sampled one point for the 100% oxygen condition due to difficulties in thermophoretic sampling. Figure 36 shows a plot of soot primary particle diameter vs. the axial centerline HAB for the soot samples in a methane flame with air (21% oxygen), 50% oxygen, and one data point for 100% oxygen. These researchers used Z to denote axial HAB and saw it on the x-axis of the figure. Their data was used for comparison to the soot primary particle diameters obtained at 100% oxygen for this work.

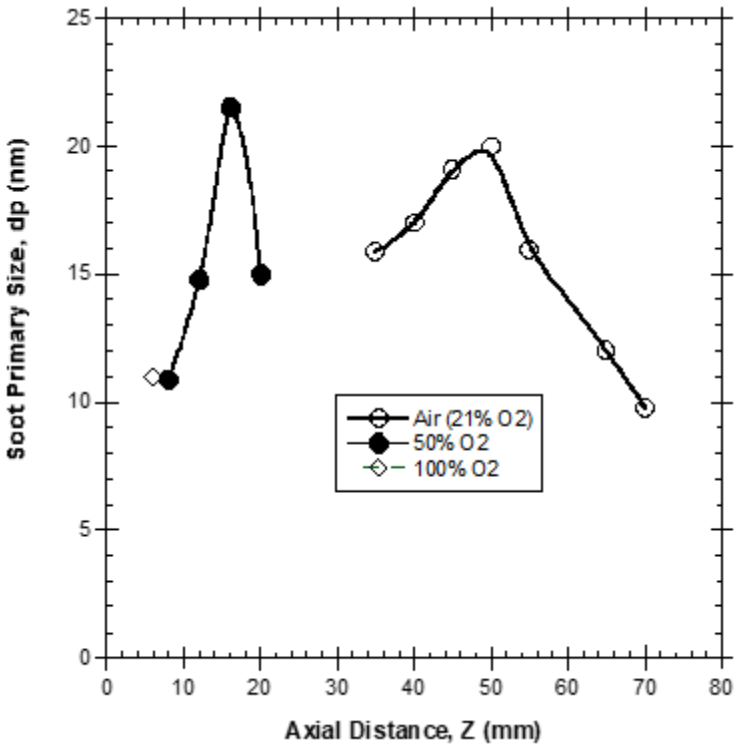

Figure 34: Soot Primary Particle Diameter as a Function of HAB in a Methane Flames with 21% Oxygen, 50% Oxygen, and 100% Oxygen [21]

For the air (21 % oxygen flame), at the first HAB sampled, the soot primary particle diameter is around 16 nm. As the HAB was increased, the primary particle diameter increased to a maximum point around 20 nm in diameter. After this maximum the dp sharply downturns until sampling stopped at the top of the flame, where the primary particle diameter was around 10 nm. For the methane/50% oxygen flame, the first sampled HAB of 10 mm had a primary particle diameter of around 11 nm. As HAB increased, d_p increased to a maximum of around 21.5 nm. The d_p then sharply decreases to the final sample with a value of about 15 nm. The only point sampled by the researchers had a d_p value of around 11 nm. One of the goals of this work was to expand on this dataset by utilizing the H2 finder grid previously discussed to allow for more detailed sampling of methane/100% oxygen flames.

For the methane/100% O_2 flame, primary particle diameters were measured from soot samples extracted at various HABs. The diameters were measured from the medium resolution TEM images using Adobe Photoshop. This provided diameters in pixels, which were then converted to

distances via the image scale bar. Figure 37 shows d_p versus axial distance HAB for the methane/100% O_2 flame studied.

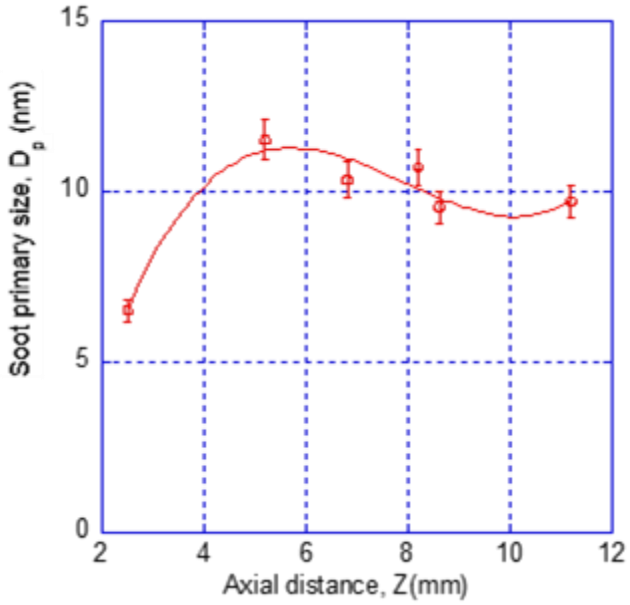

Figure 35: Soot Mean Primary Particle Diameter as a Function of HAB in a Methane/100 % Oxygen Flame. Error Bars Represent 1 Standard Deviation from the Mean

The methane/100 % O_2 flame showed a similar d_p trend as the methane/air flame and methane/50% oxygen flames studied by Lee et al. All three flames showcased an increase in diameter, an inflection point, and a maximum value, and then a decrease towards the top of the flame. The methane/100% flame studied in this work started at a d_p of about 7 nm, increased to a maximum of about 12 nm, and then steadily decreased again. This flame also shows smaller variation in overall d_p, and most of the values are lower or equal to any of the d_p values measured for the methane/air or methane/50% oxygen flame. Both the lower variance and lower measured d_p values are to be expected, as with the highest oxygen content, the soot produced in the methane/100% oxygen flame experiences more oxidation, meaning it will showcase smaller soot. This flame is also much shorter, meaning less residence time in the flame and therefore less time for growth or oxidation. This explains the lower variation in d_p for this flame. It is worth noting that the maximum d_p found here matches well with that of the d_p value found by Lee et al., which is the only d_p they presented in their work for a methane/100 % O_2 flame environment. This suggests that the measurements taken for this work meaningfully contribute to this dataset.

6.3 Soot Nanostructure Metrics for Methane/100% Oxygen Flames

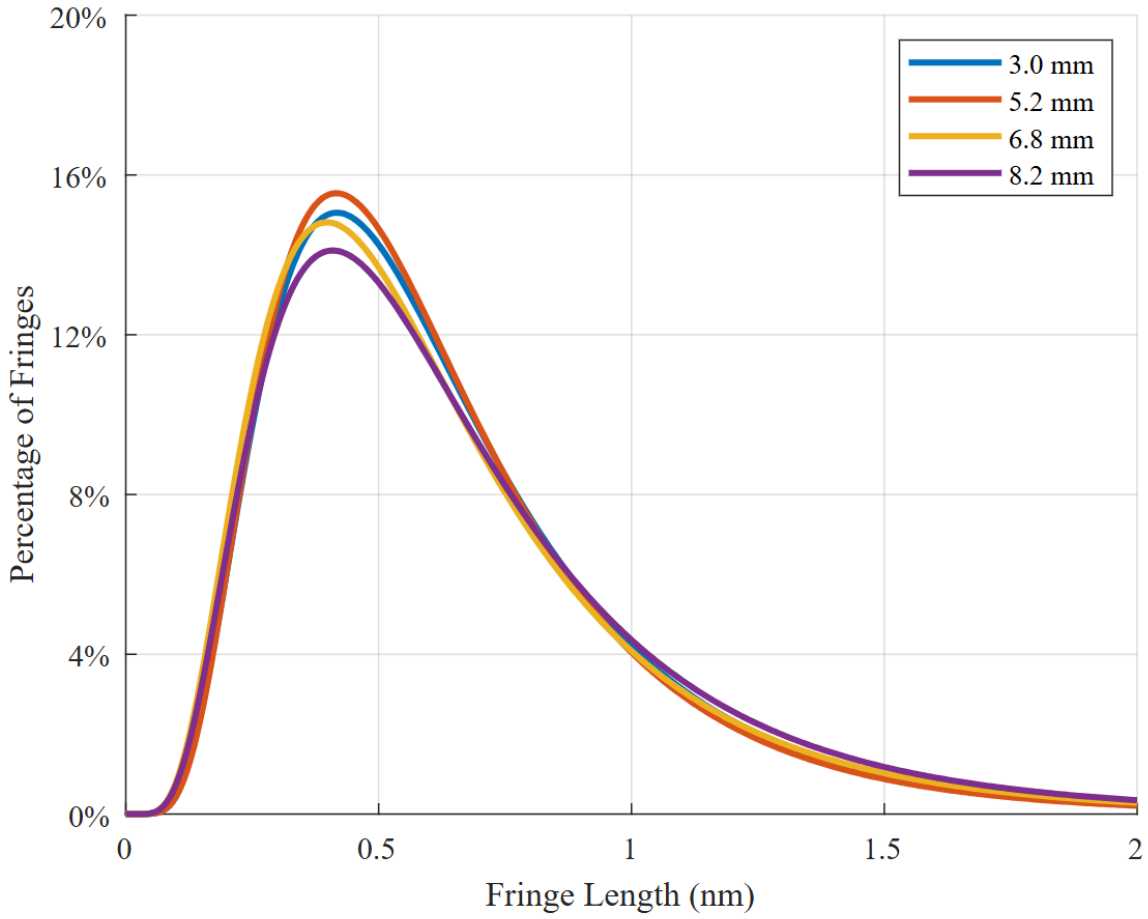

Figure 36: Log-Fit Histograms for Methane/100% Oxygen Flame

Figure 38 illustrates the log-fit distributions for fringe length for different HABs sampled in the methane/oxygen flame. Like the methane/air flame, the distributions show right-skewed behavior, meaning that most fringes for all HAB tend to be short. The distributions also show good agreement in shape, like the methane/air flame. These distributions differ from that of the methane/air flame as they peak slightly higher in fringe length, 0.4-0.5 nm, as compared to 0.34-0.35 nm. They also show lower percentages of short fringes at the peak, 14-16% of fringes when compared to the 25-27% peaks for methane/air flame distributions. There is also no discernible trend in fringe length in the methane/oxygen distribution with respect to HAB, whereas the methane/air flame shows a slight increase in fringe length with increased HAB.

Table 9. Descriptive Statistics for Fringe Length Measurements in Methane/100 % Oxygen Flames

HAB (mm)	FL (nm)	σ (nm)	σ/FL
3.0	0.67	0.47	0.70
5.2	0.65	0.43	0.66
6.8	0.67	0.50	0.75
8.2	0.69	0.50	0.71

Table 9 lists various statistical metrics used to analyze fringe length changes at various HAB for the methane/oxygen flame tested. Mean fringe length at each HAB can be seen in the second column of the table. The mean fringe lengths vary from 0.65 nm to 0.69 nm with no discernible effect from HAB. These values are noticeably higher than those of the methane/air flame. The standard deviation and coefficient of variance are also higher for the methane/oxygen flame, suggesting greater heterogeneity in fringe lengths.

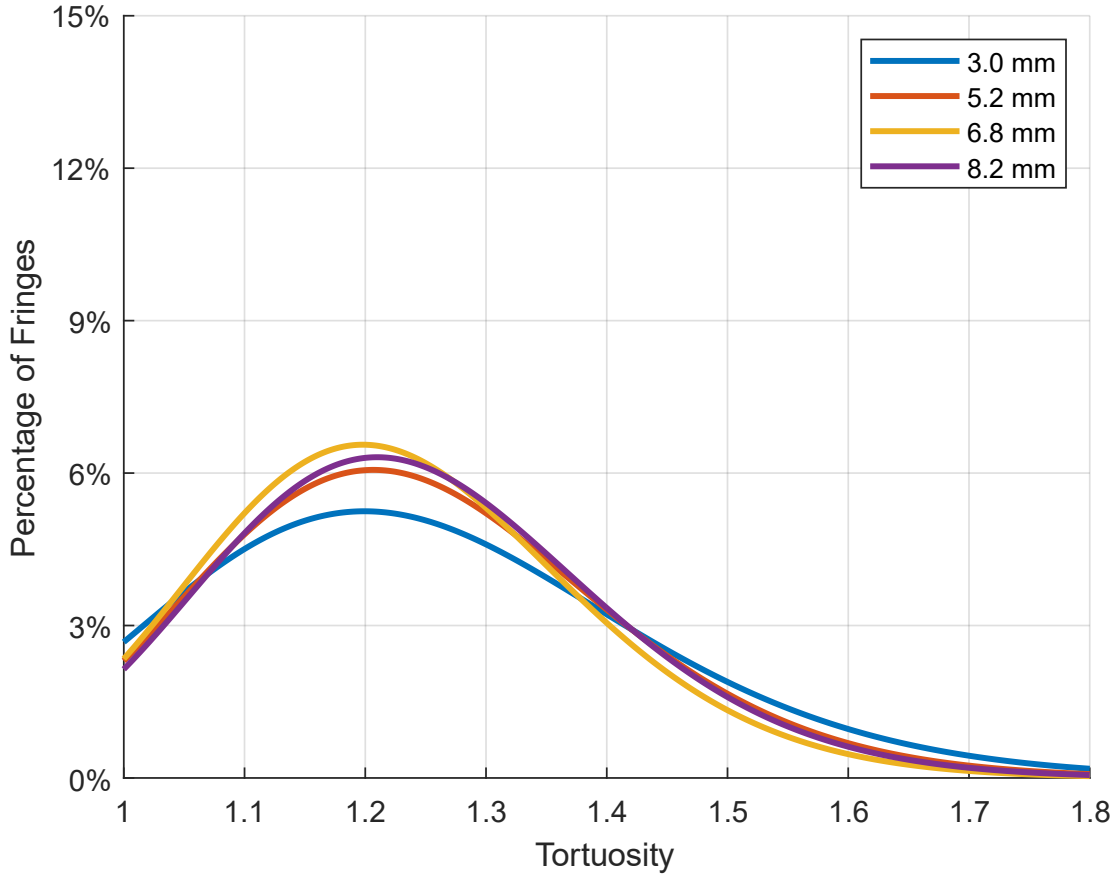

Figure 37: Log-Normal Fit of Tortuosity for Methane/100% Oxygen Flame

Figure 39 illustrates the log-fit distributions for the mean tortuosities for the sample HABs in the tested methane/oxygen flame. The distributions share a similar shape with respect to varying HAB. The lowest HAB sampled, 3.0 mm, has a slightly lower peak as compared to the rest of the distributions. This suggests that low in the flame, fringes are more tortuous, with an initial change in tortuosity as HAB increased before leveling out further into the flame.

Table 10. Descriptive Statistics for Fringe Tortuosity Measurements in Methane/100% Oxygen Flames

HAB (mm)	FT (nm)	σ	σ/FT	% FT > 1.5
3.0	1.250	0.33	0.265	5.0
5.2	1.244	0.29	0.235	4.5
6.8	1.230	0.26	0.213	3.2
8.2	1.245	0.31	0.249	3.7

Table 10 showcases statistical metrics for tortuosity at various HAB for the methane/air flame. There is little change seen in the mean tortuosity with respect to HAB; however, the percentage of fringes with a tortuosity greater than 1.5 slightly decreases with increased HAB, suggesting that the soot fringes are more disordered and curled earlier in the flame, and become more ordered as HAB increases.

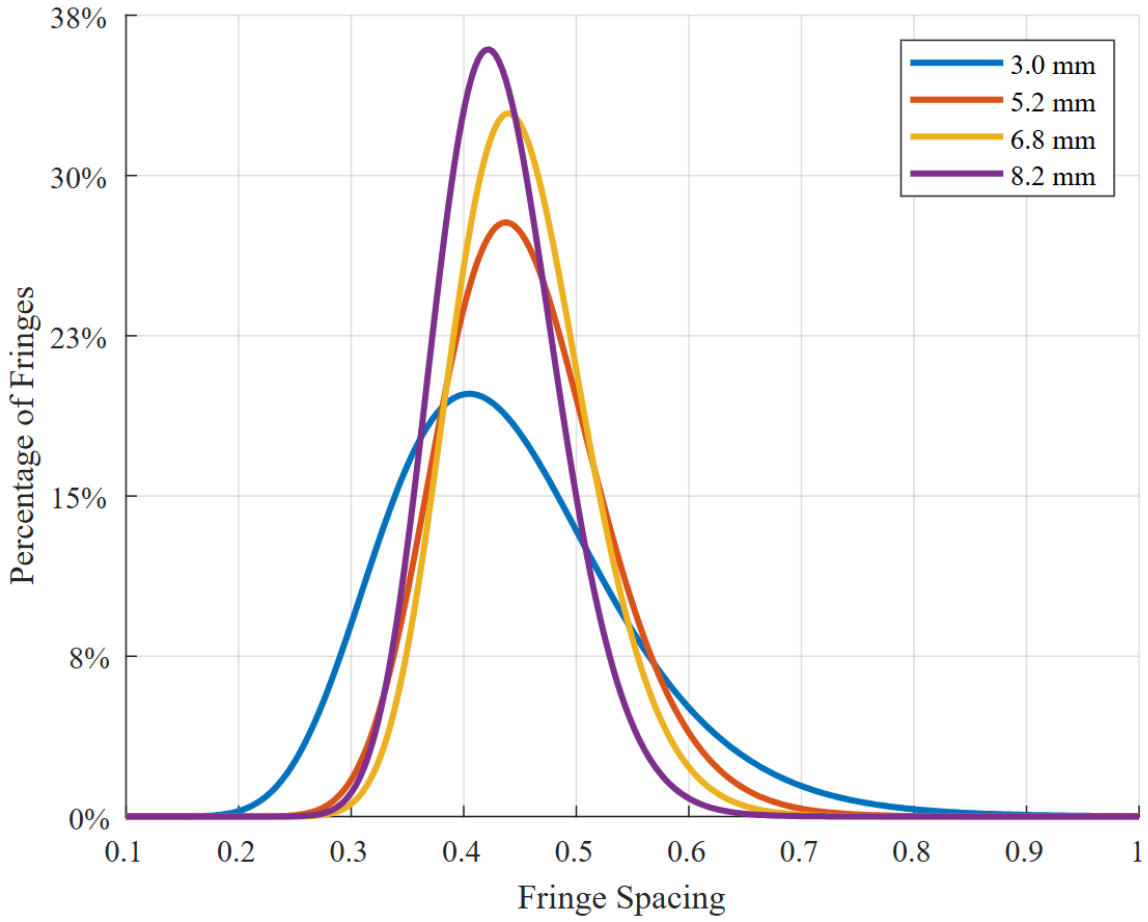

Figure 38: Statistical Metrics for Fringe Spacing Methane/Oxygen Flame

Figure 40 shows the log-fit distributions for fringe lattice spacings at various HAB for the methane/oxygen flame. The distributions show uniform shapes, but unlike the methane/air flames, they present different trends. With increased HAB, higher percentages of lower fringe lengths are observed, indicating fringes are shortening with flame height. Above 3.0 mm HAB, there is good agreement in the distributions, suggesting the fringe spacing evolves quickly and then remains relatively constant. This is also apparent in the mean fringe spacings in Table 11

Table 11. Descriptive Statistics for Fringe Lattice Measurements in Methane/100% Oxygen Flames

HAB (mm)	FS (nm)	σ	σ/FS
3.0	0.438	0.076	0.174
5.2	0.455	0.078	0.171
6.8	0.452	0.063	0.139
8.2	0.452	0.061	0.142

Table 11 shows statistical metrics for fringe lattice separation with respect to HAB for the methane/oxygen flame. The mean fringe spacing shows very little variation with respect to HAB, except for an initial increase in the mean spacing value from the base of the flame, 3.0 mm, to the next HAB, 5.2 mm. The standard variation shows an overall decrease with increased HAB, and the coefficient of variation shares a similar trend.

Chapter 7: Conclusions and Future Work Considerations

7.1 Conclusions

Low, medium, and high-resolution TEM images were used to investigate soot prosperity, nanostructure, and flame temperature metrics for a methane/air and a methane/100 % oxygen flame. The metrics of interest include soot evolution profiles, qualitative population density, degree of agglomeration of aggregates, primary particle diameter, fringe length, fringe tortuosity, fringe lattice spacing, and flame temperature. These metrics were investigated based on two dependent variables, HAB and oxygen content of the flames' oxidizer streams.

For both the methane/air and methane/100% oxygen flames, population densities and degree of agglomeration show similar trends to one another with respect to HAB. Both flames show an

initial increase with increased HAB in population density, the reaching of a maximum, and then a decrease towards the top of the flame. The methane/100% oxygen flame, however, shows noticeably less soot aggregates present at all HABs. Both flames also show similar trends regarding the degree of agglomeration of aggregates. Aggregates low in the flames are seen to start as single soot particles, grow into aggregates of multiple primary particles, reach a maximum aggregate chain length, and then begin to decrease, with the methane/100 % oxygen showing smaller aggregates overall. These trends match well with the findings of previous studies and suggest similar soot formation/evolution processes in both flames, but with the increased oxygen content, less and smaller soot is formed, likely due to increased oxidation in this flame environment.

Effects of HAB and oxygen concentration on soot primary particle diameter were investigated for a methane/100% oxygen flame, and compared to methane/air primary particle measurements taken by Lee et al. It was found that the primary particle diameter in methane/100% oxygen flames follows similar trends to those measured in methane/air flames. That is an initial increase in primary particle diameter with increasing HAB, followed by a maximum, and then a decrease. This suggests that methane/100% oxygen flames contain the same balance of soot mechanisms, that being soot inception and soot oxidation, that cause this behavior in methane/air flames. It was also observed that the soot primary particle diameter in the methane/100% oxygen flame was about half of that of its air counterpart. This affirms the belief that high oxygen content leads to more oxidation, and therefore less soot.

Next, soot nanostructure evolution profiles from HRTEM images were qualitatively analyzed. For both tested flames, soot particles are seen to be comprised of concentric graphene planes, known as fringes. Early in both flames, soot is composed of amorphous bundles of fringes, with little internal order. As the soot rises through the flame, it is seen to develop longer, more ordered fringes very rapidly, but then the order of structure does not change much after this initial ordering.

HRTEM images were then processed via in-house developed MATLAB scripts to analyze fringe length, fringe tortuosity, and fringe lattice spacing. Regarding increased HAB, the methane/air

flame showed very little change in any fringe metric, except that the mean fringe length increased from 30 mm to 40 mm HAB. After 40 mm HAB, the mean fringe length stays relatively constant. For the methane/100% oxygen flame, fringe metrics also do not vary much with HAB, except the mean fringe spacing increases from 3.0 mm to 5.2 mm HAB, but then does not change much higher in the flame. This suggests that soot produced in methane flames of any oxygen content in non-graphitizing or at least graphitizes early in the flame and only changes by outer surface growth and attachment of other primary particles, which has been seen in other research.

Next, fringe metrics between the methane/air and methane/100% oxygen flames were compared to assess the potential effect of oxygen content on the soot's nanostructure. The only metric that showed any difference between the flames was the mean fringe lengths. The mean fringe lengths for the air flame are all around 0.45 nm, while those for the methane/ 100% oxygen flame are all around 0.67 nm. This constitutes approximately 49% increase between the two flame conditions. This would be consistent with the expectation that higher oxidation rates due to higher oxygen content help to graphitize the soot present, except it would also be expected that fringe tortuosity and fringe spacing change as well, especially tortuosity, since it is known that oxidation preferably attacks more curved fringes. This is an unexpected result and could be due to the increased temperature in the methane/100 % oxygen flame promoting fringe growth at a faster rate than changes in other metrics that are expected to be seen if oxidation was the main mechanism.

Lastly, flame temperature measurements were taken at various HABs in the methane/air flame. It was found that the uncorrected flame temperature increases from 10 mm to 30 mm HAB, is relatively unchanged from 30 mm to 60 mm HAB, and then increases again after 60 mm HAB. This correlates well with temperature trends for other hydrocarbons testing in other works.

7.2 Future Work Recommendations

Some future work considerations are as follows:

1. Refinement of fringe algorithms to reduce potential sources of error: user-introduced error from manual selection of fringe pairs and distance scale setting.
2. Normalization of sampled HABs in flames of various conditions to facilitate better comparison between flame conditions.
3. Flame temperature measurements of methane/100% oxygen flames to quantify temperature increases due to higher oxygen content. This could allow insight into the mechanisms governing nanostructure formation and evolution within these flames.

References

[1] IEA, World Energy Balances: Overview. Paris: IEA, 2021. [Online]. Available: https://www.iea.org/reports/world-energy-balances-overview. License: CC BY 4.0.

[2] S. R. Turns, An Introduction to Combustion: Concepts and Applications. New York, New York: McGraw-Hill, 2012.

[3] Ultimate Diesel Tuning, "Does good quality fuel avoid engine soot build up?," Ultimate Diesel Tuning, https://ultimatedieseltuning.com.au/does-good-quality-fuel-avoid-engine-soot-build-up/ (accessed Mar. 31, 2025).

[4] Z. Li et al., "A kinetics mechanism of NOx formation and reduction based on density functional theory," Science of The Total Environment, vol. 867, p. 161519, Apr. 2023. doi:10.1016/j.scitotenv.2023.161519

[5] The atmosphere | National Oceanic and Atmospheric Administration, https://www.noaa.gov/jetstream/atmosphere (accessed Mar. 31, 2025).

[6] Z. Zhang et al., "Overview of the impact of oxygenated biofuel additives on soot emissions in laboratory scale," Fuel Processing Technology, vol. 254, p. 108046, Feb. 2024. doi:10.1016/j.fuproc.2024.108046

[7] C. E. Baukal, Oxygen-Enhanced Combustion. Hoboken: CRC Press, 2013.

[8] Mat. Integrity, "Exchanger's tubesheet thermal fatigue cracking," Exchanger's Tubesheet Thermal Fatigue Cracking, https://matintegrity.wixsite.com/inspection-corrosion/post/exchanger-s-tubesheet-thermal-fatigue-cracking (accessed Apr. 7, 2025).

[9] K. SAITO, F. A. WILLIAMS, and A. S. GORDON, "Effects of oxygen on soot formation in methane diffusion flames," Combustion Science and Technology, vol. 47, no. 3–4, pp. 117–138, May 1986. doi:10.1080/00102208608923869

[10] R. A. Dobbins and C. M. Megaridis, "Morphology of flame-generated soot as determined by thermophoretic sampling," Langmuir, vol. 3, no. 2, pp. 254–259, Mar. 1987. doi:10.1021/la00074a019

[11] “Carbon film on Thin Bar Square Mesh Grids,” Electron Microscopy Sciences: Carbon Film on Thin Bar Square Mesh Grids, https://www.emsdiasum.com/2-carbon-film-only-5 (accessed Apr. 8, 2025).

[12] P. Shen et al., “Chapter 2 – ET,” Cryo EM 101, https://cryoem101.org/chapter-2-et/ (accessed Apr. 8, 2025).

[13] Biolyst, “TEM Grids | transmission electron microscopy grids | EMS,” Electron Microscopy Sciences, https://www.emsdiasum.com/microscopytemgrids (accessed May 4, 2025).

[14] S. V. Prado Carbonell, thesis, Share OK, Oklahoma City, 2021

[15] DwyerOmega, Omega Engineering, https://www.omega.co.uk/prodinfo/thermocouples.html (accessed May 5, 2025).

[16] University of Kashmir, Planck’s radiation law, http://gdckulgam.edu.in/Files/f07ef270-7e91-4716-8825-2966f17cc0f7/Menu/Plancks_Radiation_law_3da32a73-3848-4135-bd19-e110bd2dfdbd.pdf (accessed Apr. 11, 2025).

[17] R. E. Bentley, Handbook of Temperature Measurement. Singapore: Springer, 1998.

[18] PYRO Micro-Therm, DISAPPEARING FILAMENT TYPE OPTICAL PYROMETER, https://www.pyrometer.com/dl.php?f=brochure-micro-therm&h=7dbcd394a19c933L2hvbWUvc3N0ZWlnZXIvcHVibGljX2h0bWwvc3RvcmFnZS9mdHAvaXRzL0lUUy/DtmZmZW50bGljaGVyIEJlcmVpY2ggZnJlaWVyIFp1Z2FuZy9lbi9QWVJPIFByb3NwZWt0ZS9CUiBNaWNyby1UaGVybV9JRDI3NzhfZW4ucGRm (accessed Apr. 10, 2025).

[19] A. Beltrame et al., “Soot and no formation in methane–oxygen enriched diffusion flames,” Combustion and Flame, vol. 124, no. 1–2, pp. 295–310, Jan. 2001. doi:10.1016/s0010-2180(00)00185-1

[20] J. Xi, G. Yang, J. Cai, and Z. Gu, “A review of recent research results on soot: The formation of a kind of carbon-based material in flames,” Frontiers, https://www.frontiersin.org/journals/materials/articles/10.3389/fmats.2021.695485/full (accessed Apr. 8, 2025).

[21] K.-O. Lee et al., “Soot formation effects of oxygen concentration in the oxidizer stream of Laminar Coannular nonpremixed methane/Air Flames,” Combustion and Flame, vol. 121, no. 1–2, pp. 323–333, Apr. 2000. doi:10.1016/s0010-2180(99)00131-5

[22] S. A. Zelepouga, A. V. Saveliev, L. A. Kennedy, and A. A. Fridman, “Relative effect of acetylene and PAH’s addition on soot formation in laminar diffusion flames of methane with oxygen and oxygen-enriched air,” Combustion and Flame, vol. 122, no. 1–2, pp. 76–89, Jul. 2000. doi:10.1016/s0010-2180(00)00104-8

[23] W. Merchan-Merchan, S. McCollam, and J. F. Pugliese, “Soot formation in diffusion oxygen-enhanced biodiesel flames,” Fuel, vol. 156, pp. 129–141, Sep. 2015. doi:10.1016/j.fuel.2015.04.011

[24] K. SAITO, F. A. WILLIAMS, and A. S. GORDON, “Effects of oxygen on soot formation in methane diffusion flames,” Combustion Science and Technology, vol. 47, no. 3–4, pp. 117–138, May 1986. doi:10.1080/00102208608923869

[25] Ö. L. Gülder, “Effects of oxygen on soot formation in methane, propane, and N-butane diffusion flames,” Combustion and Flame, vol. 101, no. 3, pp. 302–310, May 1995. doi:10.1016/0010-2180(94)00217-g

[26] S. Deal, D. Merchan-Breuer, A. Abdihamzehkolaei, S. Srivastava, and W. Merchan-Merchan, “Soot morphology emitted from vaporized canola methyl ester (CME) - and diesel-with varying levels of oxygen enhancement in co-flow diffusion flames,” Journal of the Energy Institute, vol. 119, p. 101935, Apr. 2025. doi:10.1016/j.joei.2024.101935

[27] S. J. Harris and A. M. Weiner, “Soot particle growth in premixed toluene/ethylene flames,” Combustion Science and Technology, vol. 38, no. 1–2, pp. 75–87, Jun. 1984. doi:10.1080/00102208408923764

[28] E. R. RAMER, J. F. MERKLIN, C. M. SORENSEN, and T. W. TAYLOR, “Chemical and optical probing of premixed methane/oxygen flames,” Combustion Science and Technology, vol. 48, no. 5–6, pp. 241–255, Aug. 1986. doi:10.1080/00102208608923895

[29] A. Beltrame et al., “Soot and NOx formation in methane–oxygen enriched diffusion flames,” Combustion and Flame, vol. 124, no. 1–2, pp. 295–310, Jan. 2001. doi:10.1016/s0010-2180(00)00185-1 (This is mentioned earlier so this needs to be made a cross referene)

[30] R. J. Santoro, T. T. Yeh, J. J. Horvath, and H. G. Semerjian, “The transport and growth of soot particles in laminar diffusion flames,” *Combustion Science and Technology*, vol. 53, no. 2–3, pp. 89–115, Jun. 1987. doi:10.1080/00102208708947022

[31] “Should it be called ‘natural gas’ or ‘methane’?,” Yale Program on Climate Change Communication, https://climatecommunication.yale.edu/publications/should-it-be-called-natural-gas-or-methane/ (accessed Jul. 3, 2025).

[32] R. A. Dobbins and C. M. Megaridis, “Morphology of flame-generated soot as determined by thermophoretic sampling,” *Langmuir*, vol. 3, no. 2, pp. 254–259, Mar. 1987. doi:10.1021/la00074a019

[33] K. Yehliu, R. L. Vander Wal, and A. L. Boehman, “Development of an hrtem image analysis method to quantify carbon nanostructure,” *Combustion and Flame*, vol. 158, no. 9, pp. 1837–1851, Sep. 2011. doi:10.1016/j.combustflame.2011.01.009

[34] M. L. Botero, D. Chen, S. González-Calera, D. Jefferson, and M. Kraft, “HRTEM evaluation of soot particles produced by the non-premixed combustion of liquid fuels,” *Carbon*, vol. 96, pp. 459–473, Jan. 2016. doi:10.1016/j.carbon.2015.09.077

[35] M. L. Botero, J. Akroyd, D. Chen, M. Kraft, and J. R. Agudelo, “On the thermophoretic sampling and Tem-based characterisation of soot particles in flames,” *Carbon*, vol. 171, pp. 711–722, Jan. 2021. doi:10.1016/j.carbon.2020.09.074

[36] S. A. Pfau, A. La Rocca, and M. W. Fay, “Quantifying soot nanostructures: Importance of image processing parameters for lattice fringe analysis,” *Combustion and Flame*, vol. 211, pp. 430–444, Jan. 2020. doi:10.1016/j.combustflame.2019.10.020

[37] M. Alfè, B. Apicella, J.-N. Rouzaud, A. Tregrossi, and A. Ciajolo, “The effect of temperature on soot properties in premixed methane flames,” *Combustion and Flame*, vol. 157, no. 10, pp. 1959–1965, Oct. 2010. doi:10.1016/j.combustflame.2010.02.007

[38] N. Otsu, “A threshold selection method from gray-level histograms,” *IEEE Transactions on Systems, Man, and Cybernetics*, vol. 9, no. 1, pp. 62–66, Jan. 1979. doi:10.1109/tsmc.1979.4310076

[39] J. Davis, K. Tiwari, and I. Novosselov, “Soot morphology and nanostructure in complex flame flow patterns via secondary particle surface growth,” *Fuel*, vol. 245, pp. 447–457, Jun. 2019. doi:10.1016/j.fuel.2019.02.058

[40] R. Tian, Y. Zhang, S. Kook, K. S. Kim, and C.-B. Kweon, “Effect of jet fuel aromatics on in-flame soot distribution and particle morphology in a small-bore compression ignition engine,” *Fuel*, vol. 305, p. 121582, Dec. 2021. doi:10.1016/j.fuel.2021.121582

[41] M. L. Botero, D. Chen, S. González-Calera, D. Jefferson, and M. Kraft, “Hrtem evaluation of soot particles produced by the non-premixed combustion of liquid fuels,” *Carbon*, vol. 96, pp. 459–473, Jan. 2016. doi:10.1016/j.carbon.2015.09.077

[42] C. Russo *et al.*, “Probing structures of soot formed in premixed flames of methane, ethylene and benzene,” *Proceedings of the Combustion Institute*, vol. 34, no. 1, pp. 1885–1892, 2013. doi:10.1016/j.proci.2012.06.127